

1 **Brazil Current volume transport variability during 2009-2015 from a long-**  
2 **term moored array at 34.5°S**

3  
4 **M. P. Chidichimo<sup>1,2,3</sup>, A. R. Piola<sup>1,2,3,4</sup>, C. S. Meinen<sup>5</sup>, R. C. Perez<sup>5</sup>, E. J. D.**  
5 **Campos<sup>6,7</sup>, S. Dong<sup>5</sup>, R. Lumpkin<sup>5</sup>, and S. L. Garzoli<sup>5</sup>**

<sup>1</sup> Dinámica Oceánica, Servicio de Hidrografía Naval, Buenos Aires, Argentina

<sup>2</sup> Consejo Nacional de Investigaciones Científicas y Técnicas (CONICET), Argentina

8 <sup>3</sup> CNRS – IRD – CONICET UBA, Instituto Franco-Argentino para el Estudio del Clima y sus  
Impactos (UMI 3351 IFAECI), Buenos Aires, Argentina

<sup>4</sup> Universidad de Buenos Aires, Buenos Aires, Argentina

1 <sup>5</sup> National Oceanic and Atmospheric Administration, Atlantic Oceanographic and Meteorological  
12 Laboratory, Miami, Florida, USA

13 <sup>6</sup> Oceanographic Institute of the University of Sao Paulo, Brazil

14 <sup>7</sup> Dept. of Biology, Chemistry and Environmental Sciences, College of Arts and Sciences,  
15 American University of Sharjah, Sharjah, United Arab Emirates

16 Corresponding Author: M. P. Chidichimo, [mpchidichimo@hidro.gov.ar](mailto:mpchidichimo@hidro.gov.ar)

17 **Key Points:**

- 18 • The multiyear continuous absolute Brazil Current transport measured at 34.5°S has  
19 significant variability on daily to monthly time scales
- 20 • The baroclinic component accounts for the largest part of the absolute transport  
21 variance, but the barotropic variance is not negligible
- 22 • No meaningful seasonal cycle, interannual variability or trend is detected during the  
23 roughly six years of daily transport measurements
- 24  
25  
26

This article has been accepted for publication and undergone full peer review but has not been through<sup>1</sup>  
the copyediting, typesetting, pagination and proofreading process, which may lead to differences between  
this version and the [Version of Record](#). Please cite this article as doi: [10.1029/2020JC017146](https://doi.org/10.1029/2020JC017146).

This article is protected by copyright. All rights reserved.

27 **Abstract**

28

29 The Brazil Current, the western limb of the subtropical gyre of the South Atlantic Ocean, is one  
30 of the major Western Boundary Currents of the global ocean. Here, we present the first multiyear  
31 continuous daily time series of Brazil Current absolute volume transport obtained using 6+ years  
32 of observations from a line of four pressure-recording inverted echo sounders (PIES) deployed at  
33 34.5°S. The array was augmented in 2012 with two current meter-equipped PIES, and in  
34 2013 with a moored Acoustic Doppler Current Profiler on the upper continental slope. The  
35 Brazil Current is bounded by the sea surface and the neutral density interface separating South  
36 Atlantic Central Water and Antarctic Intermediate Water, which is on average at a reference  
37 pressure of  $628 \pm 46$  dbar, and it is confined west of 49.5°W. The Brazil Current has a mean  
38 strength of  $-14.0 \pm 2.8$  Sv ( $1 \text{ Sv} \equiv 10^6 \text{ m}^3 \text{ s}^{-1}$ ; negative indicates southward flow) with a  
39 temporal standard deviation of 8.8 Sv and peak-to-peak range from -41.7 to +20 Sv. About 80%  
40 of the absolute transport variance is concentrated at periods shorter than 150 days with a  
41 prominent peak at 100 days. The baroclinic component accounts for 85% of the absolute  
42 transport variance, but the barotropic variance is not negligible. The baroclinic and barotropic  
43 transports are uncorrelated, demonstrating the need to measure both transport components  
44 independently. Given the energetic high frequency transport variations, statistically significant  
45 seasonal to interannual variability and trends have yet to be detected.

46

47

48

49

50

51

52

53

54

55 **Plain language summary**

56

57 Western Boundary Currents are the most intense currents of the global ocean and are key to the  
58 redistribution of mass, heat, salt, and carbon throughout the globe. In the South Atlantic, the  
59 Brazil Current transports warm and salty waters off the South American coast towards the pole,  
60 and is a major driver of climate variability. This study presents, for the first time, multiyear  
61 continuous-in-time direct observations of the Brazil Current at 34.5°S. Roughly six years of daily  
62 measurements from moored sensors, together with high-resolution snapshots of temperature,  
63 salinity, oxygen and velocity collected during seven oceanographic cruises since 2009, provide  
64 the ability to characterize the daily to seasonal to year-to-year variability of the Brazil Current  
65 with unprecedented detail. These observations reveal strong and rapid changes in the Brazil  
66 Current on time scales as short as 14-60 days, allow quantification of the required sampling to  
67 resolve longer-term variability, and improve estimates of the Brazil Current transport. The Brazil  
68 Current variability is dominated by the east-west density variations in the water column although  
69 east-west differences in bottom pressure are not negligible. Understanding of the strength,  
70 structure, and time variability of the Brazil Current is needed to improve model representations  
71 of this important flow.

72

73 **Key words:** Brazil Current, meridional overturning circulation, volume transport, variability,  
74 transport array, observations

75

76

77

78

79

80

81

82

83

## 84 **1 Introduction**

85 The Brazil Current (BC) is one of the major Western Boundary Currents (WBCs). WBCs  
86 are essential components of the ocean circulation and understanding their short-term and long-  
87 term variability and the mechanisms that drive them is a fundamental element of oceanic and  
88 climate research (e.g., Imawaki et al., 2013; Archer et al., 2018; Todd et al., 2019; Palmer et al.,  
89 2019). While the existence of the BC has been known for nearly two centuries (e.g., Rennell,  
90 1832), and the mean circulation patterns of the current have been understood for several decades  
91 (e.g., Stramma et al., 1990; Peterson & Stramma, 1991), there are still many open questions  
92 about the temporal variability of the BC and the mechanisms that drive those variations.

93 The southward flowing BC is the western limb of the subtropical gyre of the South  
94 Atlantic Ocean, carrying relatively warm and salty waters along the continental margin of eastern  
95 South America. The BC originates in the subtropics between roughly 10°S and 15°S where the  
96 westward flowing trans-Atlantic South Equatorial Current bifurcates (e.g., Stramma et al., 1990;  
97 Stramma, 1991; Rodrigues et al., 2007) in two branches: The northern branch forms the North  
98 Brazil Current and the southern branch forms the BC. After the bifurcation, the BC flows  
99 southward along the continental margin of South America, slowly increasing its southward  
100 time-mean transport from -0.8 Sv near 10-25°S to -70 Sv at roughly 35-38°S (negative transport  
101 indicates southward flow), attributed in part due to a tight anticyclonic recirculation cell in the  
102 southwest South Atlantic to the east of the mean BC flow in the upper 1400 m (e.g., Peterson  
103 and Stramma, 1990; Stramma et al., 1990). At 36-38°S, it encounters the northward flowing cold  
104 and fresh waters of the Malvinas Current, a northward branch of the Antarctic Circumpolar  
105 Current (e.g., Vivier and Provost, 1999; Spadone and Provost, 2009; Ferrari et al., 2017) and  
106 forms the Brazil-Malvinas Confluence (BMC), which meanders off towards the east (e.g.,  
107 Gordon and Greengrove, 1986; Olson et al., 1988; Lumpkin & Garzoli, 2011). Along its  
108 southward path, the BC is located mostly over the upper continental margin, with mesoscale  
109 features impacting its mean flow and producing occasional separations from the shelf break (e.g.,  
110 Campos et al., 2000; Calado et al., 2010; Soutelino et al., 2011; Lima et al., 2016). It has been  
111 reported that the BC separates from the shelf break for the last time at about 36°S (Olson et al.,  
112 1998; Goni et al., 2011).

113 Most of the available historical estimates of the southward BC transport are geostrophic  
114 relative to pre-defined levels of no motion and are based on hydrographic observations collected  
115 in the 1980's and 1990's between 12°S to 25°S (see Peterson and Stramma, 1991). Around 20°S  
116 the BC is located close to the continental shelf, with values around -6 Sv (e.g., Peterson and  
117 Stramma, 1990; Stramma et al., 1990). Historical estimates of BC transport near 23°S to 24°S  
118 have varied from -13.2 Sv to -4.1 Sv (Garfield, 1990; Campos et al., 1995; Stramma, 1989;  
119 Zemba, 1991). More recently, geostrophic estimates from historical ship data yielded a mean  
120 transport of -5.6 Sv above 500 m at 23-26°S (Biló et al., 2014). Near 33°S-35°S the historical  
121 hydrographic transports are typically around -24 to -18 Sv (Olson et al., 1988; Peterson and  
122 Stramma, 1991; Garzoli et al., 1993; Boebel et al., 1999).

123 A few historical continuous-in-time mooring records of the BC variability do exist,  
124 although in most cases the records are short (only a few months). These historical time series  
125 generally did not include the barotropic component of the flow. Müller et al. (1998) provided the  
126 sole historical transport time series observations to directly observe the flow over the Brazilian  
127 continental slope using nearly two-year long current-meter mooring arrays between 20°S and  
128 28°S. They observed a southward deepening and strengthening of the BC, reaching down to 670  
129 m at 28°S with a transport of -16 Sv west of 45°W. Several studies have quantified the baroclinic  
130 transport component using Inverted Echo Sounders (IES) between 35°S and 38°S, finding time-  
131 mean transports of -24 Sv to -10 Sv above 800 m over time periods of fifteen and eight months,  
132 respectively (Garzoli & Bianchi, 1987; Garzoli & Garrafo, 1989; Garzoli & Simionato, 1990;  
133 Confluence Principal Investigators, 1990; Garzoli, 1993). Although other studies based on  
134 repeated expendable bathythermograph (XBT) transects (e.g., Garzoli & Baringer, 2007; Garzoli  
135 et al., 2013; Lima et al., 2016; Goes et al., 2019), surface drifters (Oliveira et al., 2009),  
136 combined hydrographic data and quasi-isobaric subsurface floats (Rodrigues et al., 2010),  
137 satellite altimetry and temperature data (Goni et al, 2011), blended products with satellite  
138 altimetry and winds (Lumpkin & Garzoli, 2011), or on combinations of Argo floats and satellite  
139 altimetry (Schmid, 2014; Schmid & Majumder, 2018) have revealed some aspects of the BC  
140 time-mean and temporal variability, they were limited either in their spatial and/or temporal  
141 coverage. As a result, much remains unknown about the spatial structure of the BC and how it  
142 varies across a range of time scales.

143

144           There is great interest in observing the BC at 34.5°S, as at this latitude the BC is close  
145 to its transport maximum based on the limited observations to date at that latitude (e.g., Stramma  
146 1989; Peterson & Stramma, 1991; Garzoli, 1993). Furthermore, on the large-scale context, this  
147 latitude marks the entrance to the subtropical South Atlantic, as it corresponds to the southern  
148 boundary of the African continent. For this reason, 34.5°S has been identified as a crucial  
149 latitude for examining the meridional transports of volume, heat, and salt due to the possibility  
150 that our current climate may be in a regime of multiple equilibria of the Atlantic Meridional  
151 Overturning Circulation (AMOC) and the need for observable transport metrics in the region  
152 (e.g., Dijkstra, 2007; Huisman et al., 2010; Drifjhout et al., 2011; Weijer et al., 2019).  
153 Observational and modeling results suggest that analysis of the boundary currents in the South  
154 Atlantic is essential to explore the local and remote forcing of AMOC fluctuations (e.g., Biastoch  
155 et al., 2008; Dong et al., 2009; Dong et al., 2011a,b; Rühls et al. 2015). While in the subtropical  
156 South Atlantic the warm upper limb of the AMOC primarily occurs at the eastern basin (e.g.,  
157 Kersalé et al., 2019), the BC is unique as it carries mass and heat southward (ie. in opposite  
158 direction of the AMOC) and recent studies have shown that changes in the BC transport  
159 contribute to low frequency variability that has been observed in South Atlantic meridional  
160 volume and heat transports (e.g., Dong et al., 2009; Dong et al., 2015). It is therefore essential to  
161 accurately quantify the BC transports and variability to close the meridional basin-wide volume  
162 and heat transport budgets in the South Atlantic (e.g., Garzoli & Matano, 2011). Furthermore, the  
163 BC variability has often been poorly resolved and/or reproduced by different models (e.g., Palma  
164 et al., 2004) and there are many open questions about the response of the BC to intensifying  
165 Southern Hemisphere westerly winds under global warming (e.g., Yang et al., 2016, 2020; de  
166 Souza et al., 2019; Drouin et al., 2021), highlighting the importance of observing and  
167 understanding the characteristics and long-term variability of the BC.

168           In recent years, observations of the BC have increased as the AMOC observing network  
169 has expanded into the South Atlantic (e.g., Garzoli et al., 2012; Meinen et al., 2013; Ansorge et  
170 al., 2014; Hummels et al., 2015; Meinen et al., 2018; Frajka-Williams et al., 2019; Kersalé et al.,  
171 2020; Herrford et al., 2021). One element of this AMOC observing network, the South Atlantic  
172 MOC Basin-wide Array (SAMBA) has been under development at 34.5°S since 2009, and is  
173 presently being used to observe daily variations in the AMOC (Meinen et al., 2013, 2018;  
174 Kersalé et al., 2020). The western boundary component of SAMBA (termed “SAMBA-West”)

175 observes the flows of the BC in the upper ocean and the Deep Western Boundary Current  
176 (DWBC) below, and these observations provide the backbone of the present study between the  
177 continental shelf and 44.5°W (Figure 1; Table 1). The initial studies using the SAMBA-West  
178 array data have concentrated their analysis on the deep limb of the flow carried by the DWBC  
179 and the abyssal flows (Meinen et al., 2012, 2017; Valla et al., 2019), and this is the first study  
180 focusing on the upper ocean currents on the western boundary.

181 The purpose of the present study is to examine the daily to interannual variability of  
182 the depth-integrated volume transport of the upper ocean, carried by the BC, by analyzing the  
183 SAMBA-West moored observations during a particularly well-observed segment of time  
184 between March 2009 and November 2015. These results will provide a better understanding of  
185 the strength, structure, and temporal variability of the upper branch of the WBCs in the South  
186 Atlantic by examining variations across a multitude of timescales with this unprecedented 6+  
187 year data set.

188

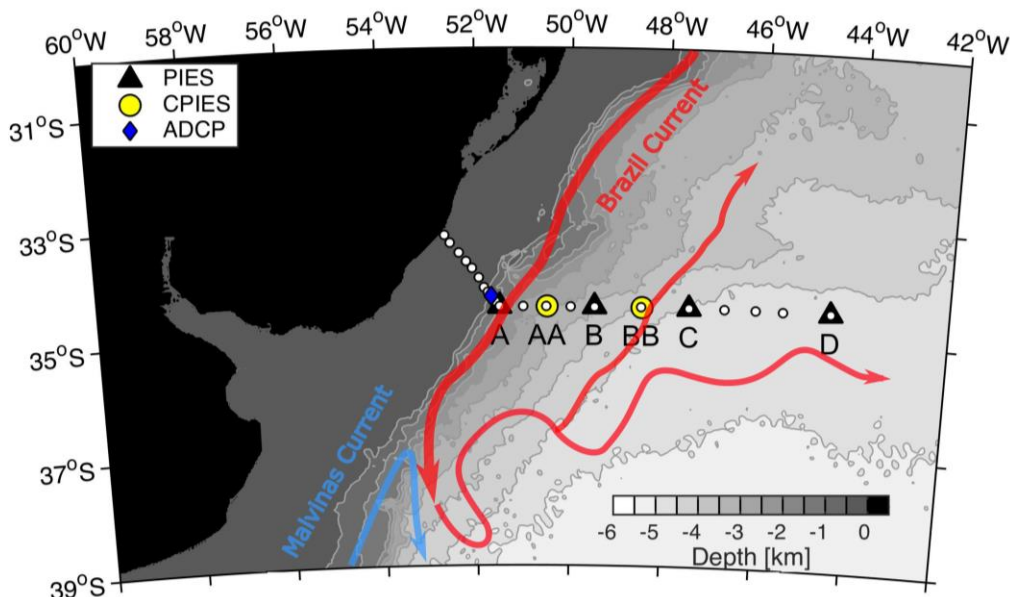
## 189 **2 Data and Methods**

190

### 191 **2.1 Overview of the SAMBA array in the western South Atlantic (“SAMBA-West”)**

192 This paper presents results from 6+ years of data from the SAMBA-West array between  
193 March 2009 and November 2015. The first component of the array was deployed in March 2009  
194 and is still operating continuously (e.g., Meinen et al., 2012, 2017; Valla et al., 2018, 2019;  
195 Kersalé et al., 2020). The SAMBA-West array was designed to study the western boundary  
196 contributions to the AMOC, and it also represents the western cornerstone of the SAMBA array  
197 which measures the basin-wide integrated meridional volume and heat transport at 34.5°S  
198 (Meinen et al., 2013, 2018; Kersalé et al., 2020). The location of the array was chosen to be just  
199 north of the meander-window for the BMC, typically found around 38°S (e.g., Gordon &  
200 Greengrove, 1986; Goni et al., 1996, 2011; Lumpkin & Garzoli, 2011), to avoid the complicated  
201 variability of the confluence front and its energetic meanders (Perez et al., 2011; Meinen et al.,  
202 2012, 2017). Initially the array consisted of a line of three pressure-recording inverted echo  
203 sounders (PIES; Sites A, C and D) moorings and one current- and pressure-recording Inverted  
204 Echo Sounder (CPIES; Site B) mooring deployed along 34.5°S spanning about 640 km between

205 the 1360-m isobath at 51.5°W (Site A; Figure 1) and the 4757-m isobath at 44.5°W (Site D;  
 206 Figure 1). The initial CPIES was later replaced with a PIES in 2011, and in December 2012 two  
 207 additional CPIES moorings were deployed between the westernmost two pairs of the existing  
 208 PIES moorings (Sites AA and BB) to improve the horizontal resolution of the array (e.g., Meinen  
 209 et al., 2017). Furthermore, in December 2013 a bottom-mounted upward looking Acoustic  
 210 Doppler Current Profiler (ADCP) mooring was deployed to capture meridional flows on the  
 211 upper continental slope, nominally at the 411-m isobath (Figure 1, Table 1). Note that the first  
 212 CPIES deployed at Site B functioned improperly in 2010 and was lost during a recovery attempt  
 213 in 2011, and as a result there is a gap of about two months at the start of the first deployment at  
 214 that site and of nearly 15 months in 2010-2011 at the end of that first deployment. The nominal  
 215 positions, water depths and deployment dates of the PIES, CPIES and ADCP moorings are given  
 216 in Table 1 (see also Figure 1).



217  
 218 **Figure 1.** Configuration of the SAMBA-West array: PIES (black triangles), CPIES (yellow  
 219 circles), ADCP mooring (blue diamond). PIES/CPIES site names on the transport line are  
 220 displayed. White circles represent the nominal positions of the hydrographic CTD/O<sub>2</sub>/LADCP  
 221 stations (Table 2). Bathymetry (shaded background) comes from the Smith & Sandwell (2007)  
 222 data set. The arrows on top represent the surface and sub-surface circulation of the Brazil Current  
 223 (red) and Malvinas Current (light blue) based on the climatological time-mean dynamic  
 224 topography (1993-2012) extracted from <https://www.aviso.altimetry.fr/>.



225 **Table 1.** Nominal positions, water depths and initial deployment dates of the instruments  
 226 distributed across the SAMBA-West transport line at 34.5°S.

Description	Site Name	Longitude (West)	Latitude (South)	Water Depth [m]	Date of first deployment
ADCP		51°40.0'	34°19.0'	411	14 December 2013
PIES	A	51°30.0'	34°30.0'	1360	18 March 2009
CPIES	AA	50°31.2'	34°30.0'	2885	11 December 2012
PIES <sup>a</sup>	B	49°30.0'	34°30.0'	3535	18 March 2009
CPIES	BB	48°30.5'	34°30.0'	4140	12 December 2012
PIES	C	47°30.0'	34°30.0'	4540	19 March 2009
PIES	D	44°30.0'	34°30.0'	4757	20 March 2009

227  
 228 <sup>a</sup> The original CPIES deployed at Site B transmitted data poorly and/or incompletely during  
 229 download cruises in August 2009, July 2010, and December 2010, so it was decided that it  
 230 would be replaced with a new PIES during the next cruise in July 2011. The CPIES was lost  
 231 during recovery, and as a result there is a gap of about two months at the start of the deployment  
 232 and nearly 15 months (21 March 2010-10 July 2011) at the end of the first deployment at that  
 233 site.

234 Between 2009 and 2015 seven cruises in support of SAMBA-West have been  
 235 conducted roughly every six to twelve months (Table 2, labelled “SAM” followed by cruise  
 236 number). During each cruise, conductivity, temperature and depth (CTD) stations were occupied  
 237 along the SAMBA-West line (white circles in Figure 1, Table 2). The SAMBA-West  
 238 hydrographic sections, which are typically collected over 4-6 days, have a typical horizontal  
 239 resolution of 20 km at the inner shelf and shelf-break and 45-90 km offshore. In addition to the  
 240 basic CTD measurements, some of the cruises also collected quasi-continuous dissolved oxygen  
 241 (O<sub>2</sub>) profiles and lowered ADCP (LADCP) measurements of full-depth velocities (data  
 242 processing is described in Valla et al., 2018, 2019). These hydrographic sections provide  
 243 independent transport estimates as we will see in section 3.2, which can be compared with the  
 244 PIES/CPIES derived transports. Three of the SAMOC-West cruises also occupied additional  
 245 stations inshore of the westernmost PIES (Site A) on the continental shelf and shelf-break,  
 246 providing an essential mean transport estimate inshore of the westernmost moored PIES at Site  
 247 A, as will be shown in section 2.2.1. An additional shelf/upper slope CTD/LADCP section was  
 248 taken in 2013 as part of the SubTropical Shelf Front (STSF) program (Berden et al., 2020; Charo

249 et al., 2020a,b). Data from the high-density XBT transect AX18, which nominally crosses the  
 250 South Atlantic along 35°S between South America and South Africa quasi-quarterly since 2002  
 251 (e.g., Garzoli & Baringer, 2007; Dong et al., 2009; Garzoli et al., 2013), are also used to compare  
 252 against the baroclinic geostrophic estimates from the PIES/CPIES array and the CTD sections.  
 253 Processing for PIES/CPIES and ADCP measurements is explained in the following subsections.

254

255 **Table 2:** Hydrography (CTD), dissolved oxygen (O<sub>2</sub>), and LADCP data used in this study.

256

Cruise	Dates	Data type	Longitude range [West]
SAM02	17-25 August 2009	CTD	51°29.0'; 44°28.0'
SAM03	5-16 July 2010	CTD/O <sub>2</sub>	51°29.0'; 44°27.0'
SAM04	20-29 December 2010	CTD	51°29.0'; 44°27.0'
SAM05 <sup>a</sup>	2-12 July 2011	CTD/LADCP	51°40.0'; 44°31.0'
SAM07	2-12 July 2012	CTD/O <sub>2</sub> /LADCP	52°50.0'; 44°31.0'
SAM08	1-16 December 2012	CTD/O <sub>2</sub>	51°38.0'; 44°29.0'
SAM10 <sup>a</sup>	4-16 October 2014	CTD/LADCP	51°31.0'; 44°31.0'
STSF	7-8 October 2013	CTD/LADCP	51°20.0'; 51°30.0'

257

258 Note. <sup>a</sup>LADCP section incomplete

259

### 260 2.1.1 PIES data processing and gravest empirical mode

261 The IES has been in use as an oceanographic tool for about 50 years (e.g., Rossby, 1969;  
 262 Watts and Rossby, 1977). In its basic form the IES measures the travel time  $\tau$  for a sound pulse  
 263 (originally 10 kHz, since the year 2000 generally 12 kHz) to travel from the sea bottom to the  
 264 surface and back. The basic processing of the raw hourly IES  $\tau$  measurements has been well  
 265 established for many years and are described in detail elsewhere (e.g., Tracey et al., 1997;  
 266 Donohue et al., 2010; Chidichimo et al., 2014). Early applications of the IES in the Southwestern  
 267 Atlantic utilized hydrography-derived relationships between dynamic height anomaly integrated  
 268 between the surface and a fixed pressure (often 300 dbar) and simulated travel time to estimate  
 269 the baroclinic transport of the upper ocean currents relative to an assumed level of no motion  
 270 (e.g., Garzoli & Bianchi, 1987; Garzoli, 1993). In the late 1980s and early 1990s, a variant  
 271 instrument integrating a bottom pressure sensor was developed (PIES; e.g. Watts et al., 1995).  
 272 The processing of the raw hourly bottom pressure data, which includes a “response analysis”

273 tidal correction following Munk and Cartwright (1966), has been presented in detail elsewhere  
274 and will not be repeated here (e.g., Watts and Kontoyiannis, 1990; Donohue et al. 2010). Later  
275 in the early 2000s a version of the instrument adding a single-depth acoustic current meter 50 m  
276 above the bottom was also developed (CPIES; e.g., Donohue et al., 2010; Bishop et al. 2012;  
277 Green et al. 2012). In essence the aforementioned papers illustrate how the hourly pressure and  $\tau$   
278 measurements are processed to produce a single daily value of  $\tau$  and pressure at noon GMT each  
279 day. Subsequently, a 72-h low-pass filter is applied to the  $\tau$  and pressure records at each site to  
280 remove tides.

281 Modern analysis of  $\tau$  data involves the use of two-dimensional look-up tables that are  
282 created via the Gravest Empirical Mode (GEM) technique developed by Meinen and Watts  
283 (2000). The details of how  $\tau$  data and bottom pressure measurements of a PIES (or CPIES) are  
284 combined with historical hydrography from the region via the use of the use of two-dimensional  
285 look-up tables that are created via the GEM technique to produce daily estimates of relative  
286 geostrophic velocity at the SAMBA-West array are presented in Meinen et al. (2012, 2013,  
287 2017) and will not be repeated here. In brief, the GEM look-up tables quantify temperature ( $T$ ),  
288 salinity ( $S$ ), and/or specific volume anomaly ( $\delta$ ) as functions of pressure and  $\tau$  calculated from  
289 hydrographic casts between the surface and a selected reference pressure (1000 dbar herein). The  
290 daily PIES-GEM estimated profiles are gridded with uniform 20 dbar pressure increments from  
291 the surface to the seafloor. The PIES-GEM  $\delta$  profiles are then vertically integrated to give daily  
292 dynamic height anomaly ( $\phi$ ) profiles relative to an assumed level of no motion. Differencing the  
293  $\phi$  profiles at neighbouring PIES/CPIES sites yields daily full water column profiles of the  
294 component of the relative geostrophic velocity perpendicular to the line between the sites (e.g.,  
295 meridional) via the standard geostrophic method (e.g., Gill, 1982). Similarly, differencing the  
296 bottom pressure measurements at neighbouring PIES/CPIES yields the temporal anomaly of the  
297 absolute geostrophic bottom velocity. However, the time mean absolute geostrophic bottom  
298 velocity cannot be determined due to the well-known leveling problem (Donohue et al. 2010;  
299 Meinen et al., 2012).

300 The products from a high-resolution numerical model are utilized to provide estimates of  
301 the time-mean bottom or reference velocities (the variability of the reference velocity comes  
302 from the bottom pressure observations). We use the time-average of 35 years of 3-day snapshots  
303 from the OGCM for the Earth Simulator (OFES) with  $0.1^\circ$  horizontal resolution and more than

304 50 vertical levels, provided by the Japan Agency for Marine-Earth Science and Technology  
305 (JAMSTEC) (e.g., Sasaki et al., 2008). Similar to previous studies in the region using data from  
306 the SAMBA-West array that have also selected this particular model run, the time-mean  
307 reference velocity was computed at 1500 dbar (Meinen et al., 2013, 2017, 2018; Valla et al.,  
308 2019).

309 Herein the time-mean meridional reference velocities used from the 35-year run from the  
310 OFES fields between 1980 and 2015 are -5.6, -6.0, 0.7, 0.7, and -0.2,  $\text{cm s}^{-1}$  between site pairs A-  
311 AA, AA-B, B-BB, BB-C, and C-D, respectively and -5.8 and 0.7  $\text{cm s}^{-1}$  between site pairs A-B  
312 and B-C, respectively. Note, our results are not sensitive to using mean OFES 1500 dbar  
313 velocities for the same period as the observations (2009-2015) vs. the 35-year mean that we used  
314 in this study.

315 Throughout this paper, we use the term “baroclinic” to refer to the transport estimated  
316 from geostrophic velocity shears referenced to zero at the bottom, and the term “barotropic” to  
317 refer to the transport contribution from the bottom-reference velocity (non-sheared term). The  
318 “absolute” transport is the sum of the baroclinic and the barotropic terms. Note that all of the  
319 time variability associated with the baroclinic and barotropic terms originate from the PIESs  
320 travel time  $\tau$  and bottom pressure measurements, respectively, and hence are independent from  
321 the model time-mean reference velocities. The time-mean of the vertically-sheared (baroclinic)  
322 term is also purely observational and independent from the model. The resulting time-mean  
323 transports are not hugely sensitive to the choice of the model to compute the time-mean  
324 meridional reference velocities (as shown in Meinen et al., 2017).

325

### 326 **2.1.2 ADCP data processing**

327 The data from the ADCP mooring deployed at 411 m depth on the upper continental  
328 slope in December 2013 (Figure 1, Table 1) were processed following standard procedures (e.g.,  
329 Côté et al., 2011). The 150 kHz ADCP recorded hourly velocity on vertical bins of 16 m, with  
330 bins centered at depths between 23.73 and 343.73 m. The hourly data were averaged to obtain  
331 daily values, and subsequently a 72-h low-pass filter was applied to remove tides.

332

333

## 334 **2.2 Absolute Brazil Current transport calculation**

335 The calculation of a boundary current transport requires a choice of the vertical and zonal  
336 limits of integration. Along the SAMBA-West array, the neutral density surface ( $\gamma^n$ ) of 27.1 kg  
337  $\text{m}^3$  separates the warm, salty, relatively low in oxygen Tropical Water (TW) and South Atlantic  
338 Central Water (SACW) from the relatively cold-fresh oxygen-rich Antarctic Intermediate Water  
339 (AAIW) located below (Valla et al. 2018; Figure 2a, b, c, d). Thus to obtain the bulk of the BC  
340 transport, we calculate transports in the depth layers occupied by the TW and SACW by  
341 evaluating the  $\gamma^n$  structure (Jackett and McDougall, 1997) across the hydrographic sections  
342 (Figure 2a, b, c; Table 2). We find the interface between SACW and AAIW on average at the  
343  $628 \pm 46$  dbar pressure level (variability represents one standard deviation; the shallowest and  
344 deepest positions observed during cruises are at 533 and 667 dbar, respectively), and we define  
345 this temporally-fixed lower bound for integrating the velocities to obtain transport. The resulting  
346 transport time series are not significantly different for modest ( $\pm 100$  dbar) changes to the 628  
347 dbar pressure level (correlation coefficient of 0.99 and root-mean-square error of 1.5 Sv). Note  
348 that at this latitude the western boundary flow is mostly southward over the entire water column  
349 so it is not possible to establish more quantitative, time-varying, criteria to separate the BC from  
350 the DWBC, such as a zero-velocity crossing. For similar reasons, Meinen et al. (2017) chose 800  
351 dbar as the upper bound to obtain the DWBC flow.

352 The definition of the horizontal limits of integration to estimate transports from in situ  
353 arrays is also not straightforward, as they strongly depend on the array's spatial resolution as well  
354 as on eddies/meanders passing by the array's laterally separated sites at each time step. Defining  
355 a static box within which a “total” (or “absolute”) BC transport will be calculated will certainly  
356 include transient transports from Rossby Waves and other features, which propagate into the  
357 integration domain. Even utilizing time-varying integration boundaries based on characteristics  
358 of the ocean flow, such as stream-coordinates, will still incorporate these other features when  
359 they superimpose on top of the main current (e.g., Meinen & Luther, 2016). As a result, the  
360 measured southward “Brazil Current” transport will fluctuate higher or lower, potentially  
361 reaching zero or even flowing northwards due to the influence of large eddies and other features  
362 (e.g., Meinen et al. 2017). For this study, the BC transport will be calculated within fixed  
363 boundaries determined from the available LADCP ship section (Figure 2e, Table 2), which as we  
364 will see later agree well with the PIES/CPIES time-mean velocity section.

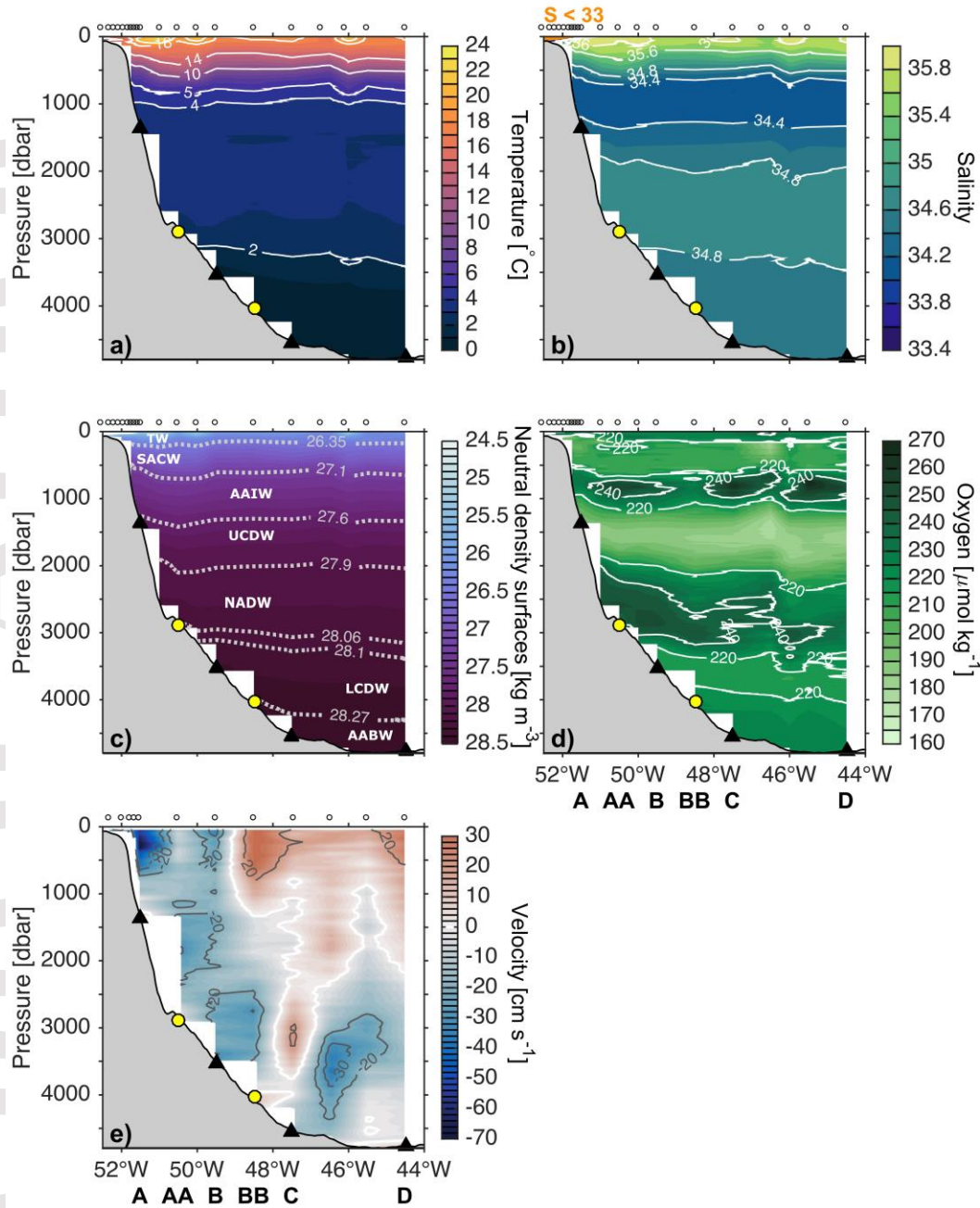
365 The full-depth spatial structure of alongshore flow from the LADCP section (Figure 2e)  
366 evidences southward flow between the shelf break and Site B (at 49.5°W) from the surface to the  
367 bottom, with the BC core at the ~100-400 dbar range near the continental slope. Offshore of Site  
368 B there is a northward recirculation. Thus, an integration domain between the coastline and Site  
369 B, and between the surface and 628 dbar (i.e., the  $\gamma^n = 27.1 \text{ kg m}^3$  surface) is selected. We will  
370 come back to the analysis of the horizontal extent of the BC in the following sections. The  
371 “absolute” BC transport represents the sum of the baroclinic and barotropic velocities integrated  
372 over this domain.

373 Note, we find that the wind-forced Ekman transport contribution to the BC in this region  
374 is very weak, and it has a very small temporal mean and standard deviation of  $-0.002 \pm 0.225 \text{ Sv}$   
375 during 2009-2015 (not shown). Additionally, the SAMBA-West array location is close to the  
376 zero value of the wind stress curl (e.g., Schmid and Majumder, 2018). Thus, we focus on the  
377 geostrophic component of the BC transport in this study.

378 To obtain the total flow above 628 dbar associated with the BC, we compute transports  
379 through two cross-sectional areas and afterwards sum them: i) over the upper continental slope  
380 inshore of the 1360 m isobath between the coast and Site A (section 2.2.1); and ii) between Site  
381 A (1360 m isobath) and Site B (3535 m isobath) (section 2.2.2).

382 Note that the full details on the estimation of the total transport accuracy is provided in  
383 Appendix A. Throughout this paper and unless otherwise noted the reported  
384 velocity/transport/pressure variability represents one standard deviation from the time-mean and  
385 negative velocities/transports indicate southward flow.

386



387

388 **Figure 2.** Average high-resolution hydrographic sections along the SAMBA-West line of (a) in  
 389 situ temperature ( $^{\circ}\text{C}$ ), (b) salinity and (c) neutral density surfaces ( $\gamma^n$ ;  $\text{kg m}^{-3}$ ) during four  
 390 hydrographic cruises (SAM05, SAM07, SAM08, and SAM10; Table 2), (d) dissolved oxygen  
 391 ( $\mu\text{mol kg}^{-1}$ ) during SAM07 and SAM08, and (e) alongshore velocity ( $\text{cm s}^{-1}$ ) derived from  
 392 LADCP velocities collected during SAM07 cruise during July 2012 (white contours indicate  
 393 zero flow; negative velocities, blue shading, indicate southward flow). A 50 m moving average is

394 applied in the vertical to the alongshore velocity profiles for stations deeper than 400 m in order  
395 to reduce noise in the LADCP data. Acronyms in panel c) indicate the key water masses after  
396 Valla et al. (2018): TW: Tropical Water; SACW: South Atlantic Central Water; AAIW:  
397 Antarctic Intermediate Water; UCDW: Upper Circumpolar Deep Water; NADW: North Atlantic  
398 Deep Water; LCDW: Lower Circumpolar Deep Water; AABW: Antarctic Bottom Water. White  
399 circles on top of the upper axis represent the nominal positions of the hydrographic CTD/O<sub>2</sub>  
400 stations (identical to Figure 1) in panels (a, b, c, d) and the positions of the hydrographic LADCP  
401 stations during SAM07 in panel (e). Gray shading is the bathymetry from the Smith & Sandwell  
402 (2007) data set. PIES and CPIES locations are indicated by the black triangles and yellow  
403 circles, respectively, on top of bathymetry of each panel. Labels at the bottom of panels d) and e)  
404 indicate the names of the PIES/CPIES sites.

405

### 406 **2.2.1 Transport on the shelf and upper continental slope**

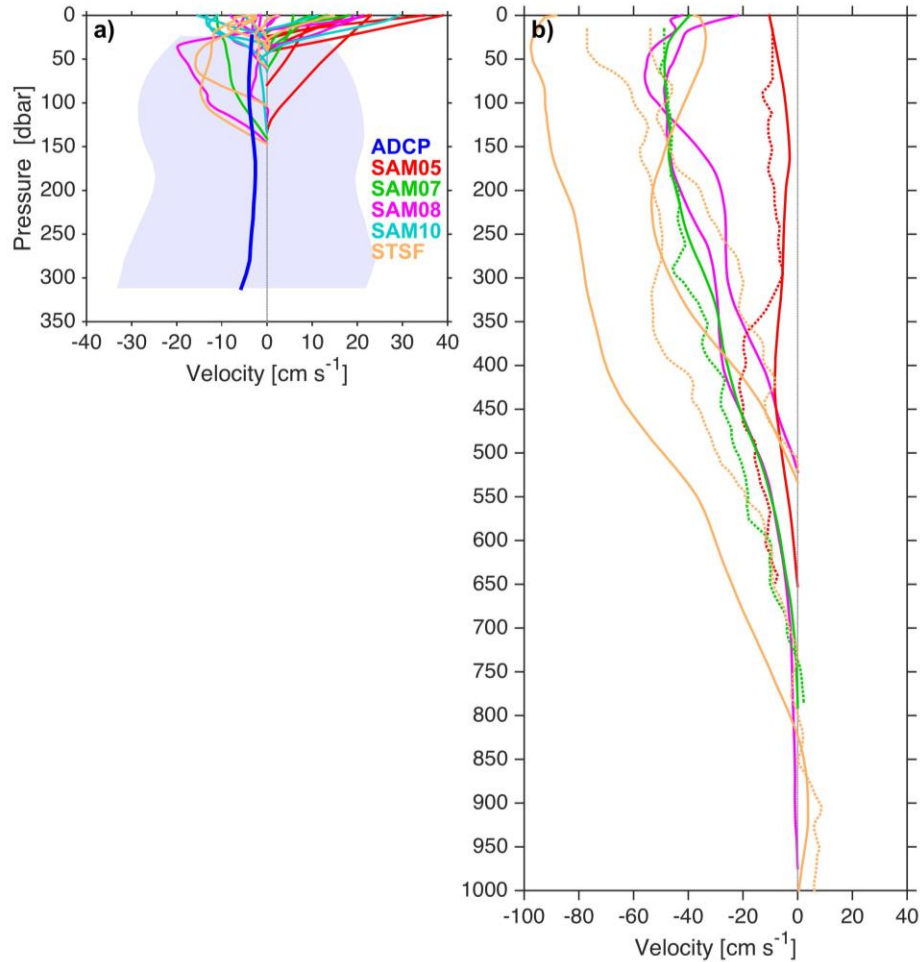
407 Due to the more limited data inshore of Site A, several different approaches were applied  
408 to estimate the transport within that wedge. A preliminary first estimate of the time-mean flow  
409 inshore of Site A was determined by evaluating the alongshore transport from the three snapshot  
410 hydrographic sections that included absolute velocity measurements with an LADCP between  
411 the 400 m isobath and Site A. Integrating the LADCP profiles from three cruises over a distance  
412 of 29 km between the 400-m isobath and Site A (1360 m isobath) and from the surface to 622 m  
413 depth gives a mean and standard deviation of the transport of  $-2.4 \pm 0.8$  Sv. A second estimate of  
414  $-2.7 \pm 1.5$  Sv was determined using all CTD data available ( $-3.0 \pm 1.8$  Sv for the three cruises  
415 that also collected LADCP observations) to estimate the velocity shear between the surface and  
416 the  $\gamma^n = 27.1 \text{ kg m}^3$  surface relative to the deepest common level (i.e., the bottom) between  
417 stations from each of the cruises that sampled between the 400 m isobath and Site A (Table 2;  
418 Figure 3b). This estimate is in good agreement with the LADCP mean estimate. The vertical  
419 structure of the CTD and the spatially-averaged LADCP shear profiles between station pairs also  
420 agree fairly well for three cruises with both types of data (see for example light green dotted and  
421 solid lines in Figure 3b).

422 Analyses of the velocity data collected with the moored ADCP at the 411-m isobath,  
423 only available between December 2013 and November 2015, provides further insights about the  
424 shelf and upper slope velocities. The time-mean flows from the ADCP (Figure 3a, blue line) are



425 weak compared to the snapshot CTD relative velocities and the LADCP absolute velocities that  
426 are found for the stations at the 500-1000-m isobath range (Figure 3b). The standard deviations  
427 of the moored ADCP velocities are quite large (Figure 3a, blue shading), however, which  
428 suggest large meridional velocity variability at this location consistent with the large spread of  
429 velocities observed during each cruise (shallow profiles on top of blue profile, Figure 3a). The  
430 mean moored ADCP velocities instead agree well in magnitude with the CTD relative velocities  
431 (solid red, light green, magenta, light blue, and orange lines) and LADCP velocities (not shown)  
432 up on the shelf for depths shallower than 200 m, which are very likely unrelated to the BC. We  
433 note that high-resolution numerical models have previously estimated weak seasonal reversing  
434 flows of  $\sim -0.4$  to  $0.3$  Sv on the continental shelf inshore the 500 m isobath near  $32^\circ\text{S}$  (Palma et  
435 al., 2008).

436 The relatively small transports in the western wedge that are not sampled by the  
437 PIES/CPIES array ( $-2.4$  Sv from LADCP;  $-2.7$  Sv from CTD) agree fairly well with previously  
438 published estimates based on long-runs of the OFES model ( $-3.0 \pm 1.6$  Sv) and the Nucleus for  
439 European Modeling of the Ocean (NEMO) model ( $-4.6 \pm 3.3$  Sv) as well as from 18 XBT  
440 sections ( $-2.1 \pm 2.5$  Sv) in Meinen et al. (2013). The limited cruise snapshot data together with  
441 the moored ADCP data suggest that the largest portion of the flow not presently sampled by the  
442 PIES/CPIES array is concentrated within the  $\sim 25$  km immediately west of Site A between the  
443 500 m and 1000 m isobaths (Figure 3b), with large southward velocities reaching up to nearly -  
444  $100$  to  $-40$   $\text{cm s}^{-1}$  in the upper 400 m of the water column during individual cruises. Figure 3b  
445 also demonstrates that the vertical structure of the velocity profiles inshore of Site A has a very  
446 “baroclinic” structure which clearly varies over time. Although a small number of snapshots are  
447 not representative of the multi-year long-term mean wedge transport, the best available option  
448 for estimating the transport within this inshore wedge is to use the average of the cruise section  
449 data. Because there are more CTD sections than LADCP sections, we have elected to use the  
450 mean CTD estimate ( $-2.7$  Sv) on the shelf-break.



451

452

453 **Figure 3.** Alongshore velocity on the shelf and continental slope inshore of Site A. a) Time-  
 454 mean velocity profile from the moored ADCP (blue line) and standard deviation (blue shading)  
 455 are shown as well as the geostrophic velocity profiles from CTD station pairs (solid red, light  
 456 green, magenta, light blue, and orange lines) for stations shallower than 400 m from the cruises  
 457 indicated in the legend. Note the absolute velocity profiles from LADCP in this region are not  
 458 shown for clarity. b) Geostrophic velocity profiles from CTD station pairs (solid red, light green,  
 459 magenta, and orange lines) and spatially-averaged absolute velocity profiles from LADCP  
 460 between station pairs when available (dotted red, light green, and orange lines) for sites between  
 461 the 500 m isobath and Site A (at 1360 m) from the cruises indicated in the legend in a). No  
 462 CTD/LADCP profiles are available in this region during SAM10. Negative velocities indicate  
 463 southward flow. Note, the different velocity scale on the x-axes for a) and b).

464

465

466 **2.2.2 Transport from PIES/CPIES**

467 The transport within the PIES/CPIES array was integrated between pairs of moorings  
468 following well-established methods (e.g., Meinen et al. 2017, and references therein; section  
469 2.1.1). Based on the meridional velocity section in Figure 2e the southward flow of the BC  
470 Current is concentrated west of 49.5°W. Sites A (at 51.5°W) and B (at 49.5°W) constitute the  
471 primary endpoints for this calculation because the records at those two sites span the longest time  
472 period (2009-2015).

473 Recall that in December 2012 two CPIES were deployed midway between Sites A and B  
474 (Site AA) and between Sites B and C (Site BB) (Figure 1, Table 1). Geostrophic flow is naturally  
475 integrating, so including an additional site between two neighbouring sites does not change the  
476 geostrophic flow integrated between the two original sites. In practice, however, transports  
477 determined using the central site or excluding the central site will not be identical in the presence  
478 of sloping bottom topography. Furthermore, the use of additional sites can reduce the size of  
479 unobserved bottom triangles along that slope. In order to test the impact of the increased  
480 horizontal resolution between Sites A and B during 2013-2015, we estimate transports between  
481 Sites A and B during those three years including Site AA. There is no significant change in the  
482 mean transport and its variability compared with the estimate excluding AA (correlation  
483 coefficient of 0.98 and root-mean-square error of 1.0 Sv) indicating that the velocity in the  
484 unobserved bottom triangles when using only Sites A and B for the calculation are very small.  
485 To test the transport contributions between Sites B and BB, we evaluate the transport from B to  
486 BB for each time step; interestingly the time-mean absolute transport between these two sites  
487 was positive (northward) during 2013-2015 ( $4.9 \pm 7.6$  Sv), which decreases the BC southward  
488 transport if included. The resulting time-mean absolute transport between Site B and Site BB in  
489 the BC depth layer when only the periods of southward flow in that span are averaged (with the  
490 condition that transports between Sites A and B are also southward) is only  $-1.0 \pm 1.6$  Sv, and  
491 would increase the southward BC transport only very slightly if included. Because Site BB is not  
492 always available during 2009-2015, we decided to only use Sites A and B as endpoints for our  
493 calculation recognizing that we may occasionally miss a minimal fraction of the BC transport  
494 offshore of Site B.

495 We determine the absolute transport BC transport as follows. First, we add a constant  
496 (time-mean) slope transport of  $-2.7$  Sv from the average of the CTD sections (section 2.2.1), to  
497 the time-varying baroclinic PIES transport time series referenced to zero at the bottom (section  
498 2.1.1), hereafter referred to as the baroclinic component of the BC transport. Next, we estimate  
499 the barotropic BC transport component as described in section 2.1.1. Finally, we combine the  
500 baroclinic and barotropic components to obtain the absolute BC transport. The resulting  
501 transport time series will be presented and discussed in the following section.

502

### 503 **3 Results and Discussion**

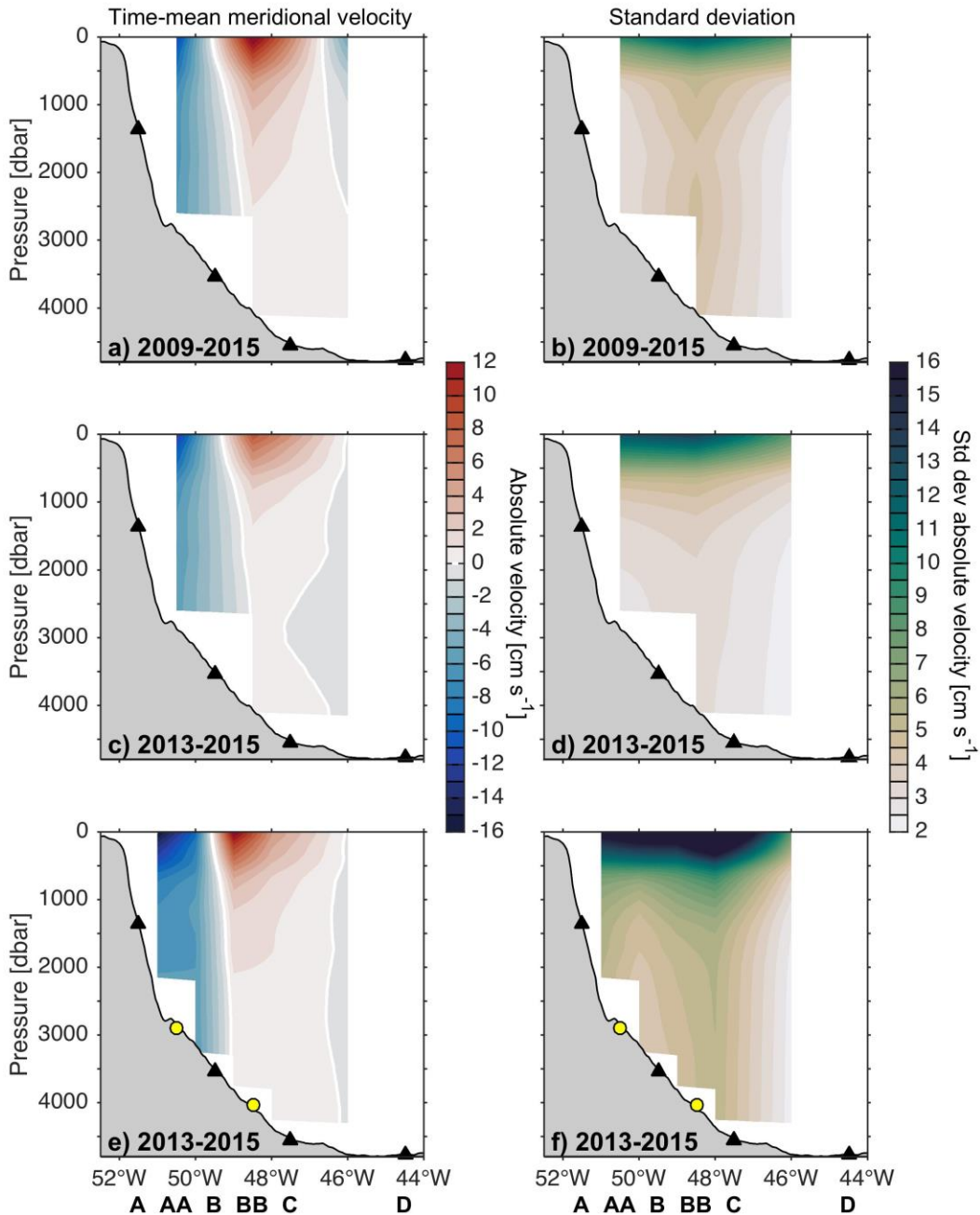
504

#### 505 **3.1 Brazil Current absolute velocity and transport variability**

506 The spatial structure of the time-mean absolute velocity section from the PIES/CPIES  
507 data shows southward flow from the surface to the ocean bottom between Sites A and B (Figure  
508 4a) with peak southward speeds reaching  $-12$  cm  $s^{-1}$  near the surface. This southward flow  
509 includes both the BC above  $\sim 628$  m (based on the density interface definition), and the DWBC  
510 below the BC base; as in previous studies with the SAMBA-West array, there is no obvious  
511 indication in the time-mean velocity field as to where one current ends and the other current  
512 begins (Meinen et al., 2012, 2017). The BC is concentrated west of  $49.5^{\circ}W$  (Figure 4a, e) in  
513 agreement with the hydrographic section (Figure 2e). When CPIES records at AA and BB are  
514 included, the peak speeds within the BC core are faster (compare Figures 4c and 4e) by  
515 approximately  $4$  cm  $s^{-1}$  between Sites A and AA, due to less horizontal averaging, but the  
516 integrated transports are very similar as is to be expected in a geostrophic calculation when  
517 velocity at the unresolved bottom triangles is small (section 2.2.2). Offshore of Site B (at  
518  $49.5^{\circ}W$ ) an evident northward recirculation can be observed in the full water column extending  
519 to  $46^{\circ}W$ , and further east of Site C the flow becomes southward again (Figure 4a, c, e) as also  
520 observed by Meinen et al. (2017) for the period 2009-2014. The temporal standard deviation of  
521 the absolute velocity profiles (Figure 4b, d, f) display large variability across the array from the  
522 surface to the bottom, with the largest variability between the surface and about 1000 dbar.  
523 When including AA and BB in the calculation, the temporal standard deviation reaches nearly 16  
524 cm  $s^{-1}$  at the BC core (comparable to the northward recirculation region) (Figure 4f). While the  
525 standard deviation provides evidence of strong surface intensification, the subsurface variability

526 of the BC is also substantial (e.g., Figure 4b) and it is further enhanced with the addition of data  
 527 from two more moorings (Figure 4f).

528



529

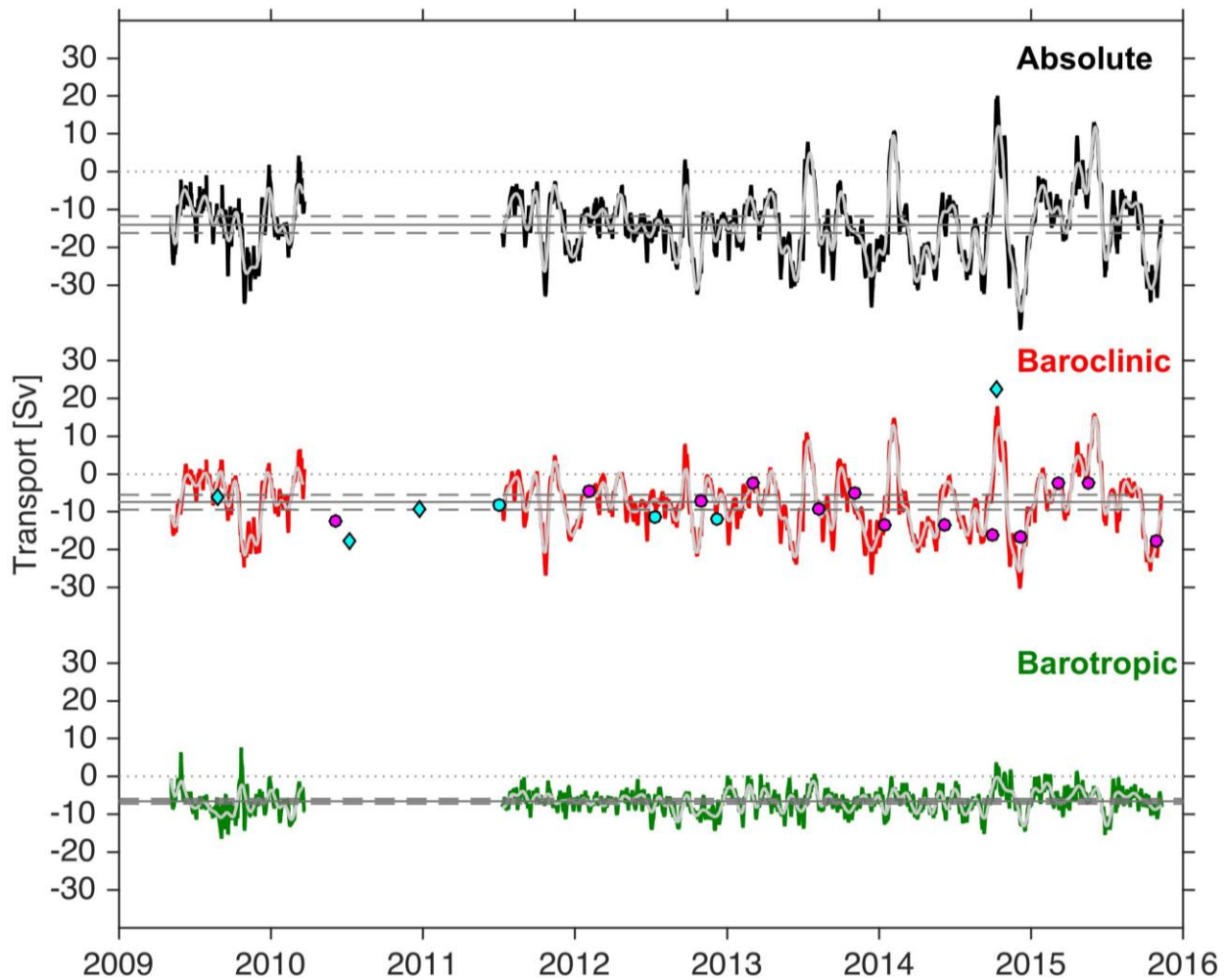
530 **Figure 4:** Time mean absolute meridional velocity between PIES/CPIES station pairs along the  
 531 SAMBA-West array (left panels) and temporal standard deviation (std dev) of the absolute  
 532 meridional velocity (right panels). The time-mean and temporal standard deviation of the

533 absolute meridional velocity are computed for (a, b) the full period of PIES measurements  
534 (2009-2015), (c, d) for the period when the horizontal resolution of the array was augmented  
535 with CPIES AA and BB but only using the PIES data (2013-2015), and (e, f) for the period when  
536 the horizontal resolution of the array was augmented with CPIES AA and BB using all available  
537 data (at Sites A, AA, B, BB, C and D) (2013-2015). White contours in left panels indicate zero  
538 flow. Negative velocity indicates southward flow. Labels at the bottom of panels e) and f)  
539 indicate the names of the PIES/CPIES sites.

540 The absolute, baroclinic, and barotropic BC transport records during 2009-2015 exhibit  
541 means and standard deviations of  $-14.0 \pm 8.8$  Sv,  $-7.4 \pm 7.6$  Sv, and  $-6.6 \pm 3.1$  Sv, respectively  
542 (Figure 5; Table 3). The Standard Error of the Mean (SEM) of the absolute transport is 1.1 Sv  
543 based on the estimated 64 degrees of freedom in the record (Appendix A). The three time series  
544 all have large temporal variability with respect to their time-mean value, consistent with what  
545 has been observed in the DWBC below/offshore of the BC (Meinen et al., 2017). There are  
546 several times when the absolute transport (black curve in Figure 5) is positive (northward) or  
547 close to zero, e.g., for the periods centered on 9 March 2010, 21 September 2012, 5 February  
548 2014, 12 October 2014 and 31 May 2015. These periods of positive (or close to zero) absolute  
549 transport are mainly due to changes in sign of the baroclinic velocity component (compare black  
550 and red curves in Figure 5). The absolute transport time series exhibits a peak-to-peak transport  
551 range of 61.7 Sv, with maximum southward flow of  $-41.7$  Sv on 6 December 2014, and  
552 maximum northward flow of 20 Sv on 12 October 2014. There is large short-term variability in  
553 the record, with changes of up to 20-30 Sv occurring over periods as short as 2-3 weeks, for  
554 instance between 24 November and 11 December 2009, 2 September and 22 September 2012, 15  
555 June and 9 July 2013, 20 January and 4 February 2014, and 17 September and 7 October 2014  
556 (black curve in Figure 5). Transport variations from peak-to-peak of  $\sim 40$ -45 Sv are observed  
557 over periods of 30-60 days, e.g., between 13 December 2013 and 4 February 2014, and 7  
558 September and 12 October 2014, and even larger peak-to-peak changes of  $\sim 50$ -60 Sv are  
559 observed between mid October 2014 and early December 2014.

560 The baroclinic transport also exhibits a large peak-to-peak transport range of 50 Sv, with  
561 similar rapid changes observed over short periods (red curve in Figure 5). The barotropic  
562 transport peak-to-peak range of 24.2 Sv is smaller than for the baroclinic record but it is still  
563 quite large. The barotropic transport also has fast changes of approximately 15 to 20 Sv during

564 short periods of time, for instance between 12 December 2012 and 2 January 2013, and 12  
 565 September 2014 and 7 October 2014 (green curve in Figure 5). As with the peak-to-peak ranges,  
 566 the standard deviation of the barotropic transport is smaller than that of the baroclinic transport  
 567 (3.1 Sv vs. 7.6 Sv, respectively). The large amplitude fluctuations in the three records persist  
 568 even after 30-day low-pass-filtering the records using a sixth order Butterworth filter applied  
 569 forward and backward to avoid phase shifts (Emery and Thomson, 2001; gray curves  
 570 superimposed on black, red and green curves, Figure 5).



571  
 572 **Figure 5.** Time series of 72-h low-pass-filtered absolute (black), baroclinic (red), and barotropic  
 573 (green) Brazil Current transport observed at 34.5°S during 2009-2015. The thin gray lines  
 574 overlaid on top of each time series are the 30-day low-pass-filtered records. The gray horizontal  
 575 solid and dashed lines indicate the time-mean and time-mean plus minus two standard errors of  
 576 the mean ( $2 \times \text{SEM}$ ; 95% confidence value), respectively. The cyan symbols indicate baroclinic

577 transports estimated from concurrent hydrographic transects during the SAMBA-West cruises  
 578 (circles and diamonds represent cruises with and without data inshore Site A, respectively; Table  
 579 2) and the magenta circles indicate the baroclinic transports computed using the measurements at  
 580 the AX18 XBT line nominally at 35°S. Negative transports correspond to southward flow.

581

582 **Table 3.** Basic statistics of the 72-h low-pass filtered absolute, baroclinic, and barotropic Brazil  
 583 Current transport between 2009 and 2015.

	Mean ± Standard Deviation [Sv]							
	2009	2010	2011	2012	2013	2014	2015	Average 2009-2015
Absolute	-14.0 ± 7.4	(-12.1 ± 6.0)	(-12.8 ± 6.9)	-14.7 ± 5.7	-14.8 ± 8.0	-16.2 ± 12.0	-10.8 ± 9.8	-14.0 ± 8.8
Baroclinic	-7.0 ± 7.0	(-4.7 ± 4.5)	(-6.9 ± 6.7)	-7.4 ± 4.8	-8.5 ± 7.4	-9.5 ± 9.7	-5.1 ± 8.2	-7.4 ± 7.6
Barotropic	-7.0 ± 3.7	(-7.4 ± 3.0)	(-5.9 ± 2.1)	-7.3 ± 2.5	-6.3 ± 2.7	-6.7 ± 3.5	-5.7 ± 3.0	-6.6 ± 3.1
	<b>Median [Sv]</b>	<b>Min [Sv]</b>	<b>Max [Sv]</b>	<b>ITS [days]/ DOF</b>	<b>SEM [Sv]</b>			
Absolute	-13.6	-41.7	20.0	12/64	1.1			
Baroclinic	-7.0	-30.2	17.8	12/64	1.0			
Barotropic	-6.5	-16.5	7.7	63/125	0.3			

584 Note. (top) The mean and standard deviation of annual and average transports are given in  
 585 columns 2-9. The mean annual values for years with less than eight months are given in brackets  
 586 (years 2010 and 2011 have three and six months of available data, respectively). (bottom) The  
 587 median, minimum and maximum values are given in columns 2-4. The integral time scale (ITS,  
 588 days) and the degrees of freedom (DOF) are given in column 5 and the standard error of the  
 589 mean (SEM) is given in column 6 (see Appendix A).

590

591 The correlation coefficient ( $r$ ) between the baroclinic and absolute transport is high ( $r =$   
 592 0.92; significant with 99% confidence, Appendix A). In contrast, the correlation between the  
 593 baroclinic and barotropic components of the transport is quite low ( $r = 0.31$ ) but significant with  
 594 95% confidence, and increases only slightly after applying a 30-day low-pass filter to both  
 595 records to remove the high frequency signals ( $r = 0.42$ ; significant with 95% confidence). The  
 596 coherence spectra between the two records indicates that the time series are moderately  
 597 correlated ( $0.40 < r < 0.50$ ) for a narrow coherence period band centered at about 100 days, but  
 598 are poorly coherent at other periods (not shown). The variability of the baroclinic component  
 599 accounts for the largest fraction of the absolute transport variability (85%), confirming that the



600 BC is mostly driven by changes in the baroclinic density field, but also indicating that the  
601 variability of the barotropic component is significant, accounting for 15% of the variance of the  
602 absolute transport.

603

### 604 **3.2 Comparison with other transport estimates**

605 Historical BC transport studies have used different methods to define the depth of the  
606 base of the current and to determine its zonal extent, and most of these studies have not  
607 accounted for the barotropic component of the flow. Therefore, comparison among the different  
608 estimates is not straightforward. Furthermore, the BC has considerable transport variations along  
609 its southward path (e.g., Olson et al., 1988; Goni et al., 2011), with baroclinic values ranging  
610 from -1.5 Sv to -4.9 Sv to -13.2 Sv at 22°S, 24°S, and 34.5°S, respectively, all calculated using  
611 data collected during the same A09 cruise in 2009 (King and Hamersley 2010; Bryden et al.  
612 2011). As such, the most useful comparison is with other measurements collected close to our  
613 mooring locations at 34.5°S. Near 37.5°S-38°S, a time-mean baroclinic transport of -10 Sv  
614 relative to and above 800 m was reported by Garzoli and Bianchi (1987) from eight months of  
615 data from two IES moorings. This value yields roughly one third larger southward flow than our  
616 time-mean baroclinic estimate of -7.4 Sv, but the difference is well within our standard deviation  
617 of 7.6 Sv. During the Confluence Program study in 1988-1990 (Garzoli, 1993), a much larger  
618 southward baroclinic transport was found, -24 Sv at 35.2°S and 36.5°S. Because these historical  
619 observations were collected a decade or more before our new results, it is difficult to know  
620 whether the observed differences are due to temporal variability between the two time periods or  
621 are the result of observational/methodological differences.

622 The highly spatially-resolved hydrographic sections taken along 34.5°S during the  
623 SAMBA-West cruises (Table 2), yield a mean and standard deviation of the transport of  $-6.6 \pm$   
624  $13.0$  Sv (cyan circles and diamonds in Figure 5), which agrees well with the PIES baroclinic  
625 transport time series mean and standard deviation of  $-7.4 \pm 7.6$  Sv (red curve in Figure 4, Table  
626 3). Note that these hydrographic CTD *T* and *S* profiles measured during the SAMBA-West  
627 cruises were not included in our GEM construction, thus allowing an independent comparison  
628 between the PIES/CPIES-derived estimates and the baroclinic transport estimates from  
629 hydrography. The even higher spatially-resolved XBT NOAA transect AX18 along 35°S (e.g.,

630 Garzoli & Baringer, 2007; Garzoli et al., 2013; Dong et al. 2015), which has been maintained  
631 since 2002, gives a mean and standard deviation for the baroclinic transport relative to and above  
632 800 m between 2010 and 2015 of  $-9.5 \pm 5.8$  Sv (the XBT transect was not occupied in 2009).  
633 Most of these XBT transects were occupied on average during periods of relatively enhanced  
634 southward flow (magenta circles in Figure 5), which explains the slightly enhanced southward  
635 baroclinic transport and highlights again the need for continuous measurements to avoid aliasing.

636 Historical estimates of the absolute transport, including both baroclinic and barotropic  
637 components of the flow, are fewer in number and have included a combination of XBTs, Argo,  
638 models, and satellite altimetry. Goni and Wainer (2001) found  $-14.0 \pm 7.0$  Sv from a  
639 TOPEX/POSEIDON ground track crossing the BC near  $35^\circ\text{S}$ , in good agreement with our  
640 measurements. At  $35^\circ\text{S}$  a combination of *in situ* data from the AX18 XBT line and a model-  
641 based barotropic adjustment yielded an absolute transport of  $-19.4 \pm 4.3$  Sv (Garzoli & Baringer,  
642 2007; Garzoli et al., 2013). More recently, meridional transports of the BC at  $35^\circ\text{S}$  in the upper  
643 800 m were estimated as  $-12.6 \pm 2.6$  Sv at  $34.5^\circ\text{S}$  using Argo and altimetry data (Schmid and  
644 Majumder, 2018). While the temporal mean values from the XBT/model adjusted and  
645 Argo/altimetry products ( $-19.4$  and  $-12.6$  Sv, respectively) are relatively close to the value we  
646 find with the SAMBA-West data ( $-14.0$  Sv), their transport standard deviations (4.3 and 2.6 Sv,  
647 respectively) are considerably smaller than what is found with the daily (8.8 Sv) or even with the  
648 30-day low-pass filtered (8.2 Sv) SAMBA-West data. This is almost certainly due to the lower  
649 sampling rates of the XBT/model adjusted (quasi-quarterly transects) and Argo/altimetry (7-10  
650 day repeats for altimetry & Argo) products. The lower sampling rates will miss the high  
651 frequency variability and rapid changes in the transport that are captured by the SAMBA-West  
652 data (section 3.1; Figures 5, 6). An additional disadvantage of the Argo-based product is that  
653 Argo data are not available on the continental shelf and upper slope, as floats are generally not  
654 deployed inshore of the 2000 dbar isobath to reduce the chances of float grounding (e.g., Riser et  
655 al., 2016). Thus Argo-based estimates will miss the portion of the BC inshore of the 2000 dbar  
656 isobath which as we have shown is a significant portion of the current (e.g., Figures 3b, 4e).

657 Our absolute time-mean transport estimate from SAMBA-West is not particularly  
658 sensitive to the choice of the reference level to compute the time-mean meridional reference  
659 absolute velocities from the high-resolution OFES run (section 2.1.1). Choosing different  
660 reference levels instead of 1500 dbar yields differences of  $-0.6$  Sv (stronger southward flow) and

661 1.7 Sv (weaker southward flow) in the resulting time-mean absolute transport when choosing  
 662 1200 dbar or 2100 dbar, respectively. Similarly, if the time-mean reference velocity at 1500 dbar  
 663 was 10% larger or 10% smaller the resulting transport estimates would differ by only -0.7 Sv  
 664 (stronger southward flow) or 0.6 Sv (weaker southward flow). Recall the OFES model is only  
 665 used to provide the time-mean reference velocity value of the non-sheared (barotropic) term, the  
 666 variability of the barotropic component is purely observational as is the time-mean and temporal  
 667 variability of the sheared (baroclinic) term (section 2.1.1).

668

### 669 3.3 Spectral distribution of energy of the observed Brazil Current transport

670

671 Band-pass filtering the time series into bands with periods shorter than 30 days, periods  
 672 between 30 and 150 days, and periods longer than 150 days shows that nearly 70% of the  
 673 absolute transport variance is associated with periods between 30 and 150 days, while periods  
 674 longer than 150 days account for only 19% of the variance, demonstrating a large variability on  
 675 monthly and shorter time scales (Table 4). Similarly, 70% of the baroclinic transport variance is  
 676 associated with periods between 30 and 150 days, while for the barotropic transport a much  
 677 larger fraction of the variance (40%) is associated with periods shorter than 30 days compared  
 678 with what is found for the baroclinic term (11%) (Table 4).

679

680 **Table 4.** Variance ( $\text{Sv}^2$ ) and % of variance explained for different period bands in the observed  
 681 absolute, baroclinic, and barotropic Brazil Current transports.

	Variance explained ( $\text{Sv}^2$ ) (Percentage)		
	3 to 30 days	30 to 150 days	More than 150 days
Absolute	9.2 (12%)	53 (69%)	15 (19%)
Baroclinic	6 (11%)	39 (70%)	11 (19%)
Barotropic	4 (40%)	5 (50%)	1 (10%)

682 Note. The statistics correspond to the period of continuous measurements between July 2011 and  
 683 November 2015 (same period used to compute the spectra in Figure 6).

684

685 In order to evaluate more precisely how the energy in these records is distributed by time  
 686 scale, the spectral frequency distributions of the transport time series were computed using the  
 687 longest portion of the records with continuous measurements (2011-2015) via Welch's

688 periodogram method using a 300-day-wide Hamming window allowing 150 days of overlap  
689 (Welch, 1967; Emery and Thomson, 2001). The spectrum of the absolute transport (Figure 6a)  
690 has a significant broad peak centered at 100 days and a much less prominent and noisier peak  
691 near 20 days. The spectrum of the baroclinic transport also has significant energy near 100 days  
692 and a secondary and noisier peak near 20 days (Figure 6b). The barotropic transport spectrum is  
693 noisier (Figure 6c) with several shorter period peaks (less than 150 days), with the most  
694 prominent peaks at 40-50 and 100 days. The large high-frequency content in all of these records  
695 highlights again the importance of continuous measurements with high temporal resolution to  
696 avoid aliasing.

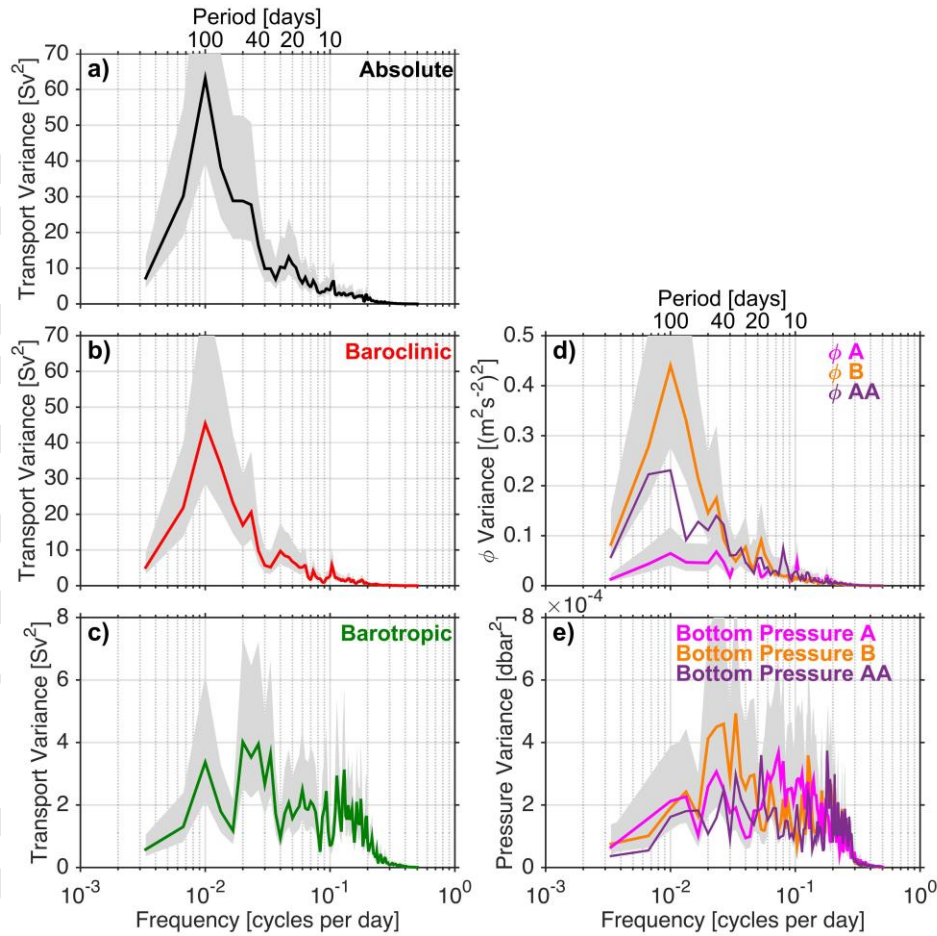
697 To further investigate the origin of the observed transport fluctuations, the spectra of the  
698 geopotential anomaly  $\phi$  and bottom pressure at Sites A and B calculated in the same manner are  
699 also shown (Figure 6d, e). Both  $\phi$  records at Sites A and B have energy near 20 days, while  $\phi$  at  
700 Site B exhibits a very distinctive broad peak centered near 100 days, thus indicating that density  
701 variations at Site B largely drive the variability of the absolute transport at this time scale. The  
702 72-h low-pass-filtered records of the absolute transport and  $\phi$  at Site B are significantly  
703 anticorrelated with 99% confidence ( $r = -0.86$ ), implying that a linear relationship between the  
704 transport and  $\phi$  at B explains nearly 74% of the absolute transport variance, while the 72-h low-  
705 pass-filtered records of the absolute transport and  $\phi$  at Site A are significantly correlated with  
706 99% confidence but the correlation decreases ( $r = 0.60$ ). Thus, observations of the density field  
707 at Site B at 49.5°W are key to the calculation of the BC transport at this latitude, but both sites  
708 are relevant in setting the time scales of variability. The spectrum of  $\phi$  at Site AA (at the 2885 m  
709 isobath midway between A and B; purple curve in Figure 6d) calculated for the period 2013-  
710 2015 also exhibits a peak near 100 days, albeit weaker than at Site B. The correlation between  
711 the  $\phi$  records at Sites AA and B is low but significant with 95% confidence ( $r = 0.31$ ), while the  
712 correlation between  $\phi$  records at Sites A and AA is much lower ( $r = 0.11$ ) and not significant.  
713 The absolute transport and  $\phi$  at Site AA are also not significantly correlated ( $r = -0.21$ ). The  $\phi$   
714 variability at Sites A and B is likely to be influenced by processes such as the variability of  
715 separation of the BC from the coast (e.g., Olson et al., 1988; Goni et al., 2011), meanders in the  
716 current itself, and eddies propagating into the mooring array and interacting with or  
717 superimposing on the current (e.g., Garzoli 1993; Meinen et al., 2017). The spectra of the bottom  
718 pressure at Sites A, AA and B have similar characteristics with an apparent common signal

719 across the sites with noisy peaks for periods shorter than 60 days, peaking most prominently at  
720 40-50 days, especially at Site B (Figure 6e). Strong bottom pressure variations at Site A at  
721 periods less than 200 days were also identified in Meinen et al. (2018).

722 In the literature, energetic short-term fluctuations (at periods of 20 to 50 days) have also  
723 been identified from observations of the baroclinic component of the BC transport near 37-39°S  
724 (Garzoli & Bianchi, 1987; Garzoli & Simionato, 1990). Near the continental slope, the most  
725 prominent signal observed was at 21 days, which they postulated was caused by a coastally  
726 trapped wind forced response. Garzoli and Simionato (1990) attributed the energy found in the  
727 band from 20 to 50 days to wave signals propagating at different periods with opposite  
728 directions, specifically a westward propagating wave associated with frontal displacements and  
729 an eastward propagating topographic Rossby Wave. Meinen et al. (2017) also noted large  
730 westward propagating Rossby Wave-like features within the SAMBA-West array.

731 The physical mechanisms responsible for the observed BC baroclinic and barotropic  
732 transport variability will be examined in a following study.

733



734  
 735 **Figure 6.** Variance preserving spectra of daily 72-h low-pass filtered a) absolute, b) baroclinic,  
 736 and c) barotropic Brazil Current transport time series. Note the different scale on the y-axes for  
 737 c). The variance preserving spectra of  $\phi$  relative to the bottom integrated in the upper layer  
 738 between the surface and the interface between TW/SACW and AAIW (on average at about 628  
 739 dbar) at Site A (magenta) and Site B (orange) are shown in d) and the variance preserving  
 740 spectra of bottom pressure at site A (magenta) and site B (orange) are shown in e). Shaded  
 741 confidence interval (95%) is also shown. The spectra of dynamic height ( $\phi$ ) and bottom pressure  
 742 at Site AA (at 50.5°W midway between Sites A and B) for the period 2013-2015 are also shown  
 743 in panels d) and c) respectively (purple lines; shaded confidence interval is not shown for clarity)  
 744 to allow comparison. Recall that the time series at Sites A and B constitute the endpoints for the  
 745 transport calculations. The spectra are computed based on Welch's periodogram method using  
 746 300-days-wide Hamming window and 150-days of overlap between consecutive data segments.  
 747

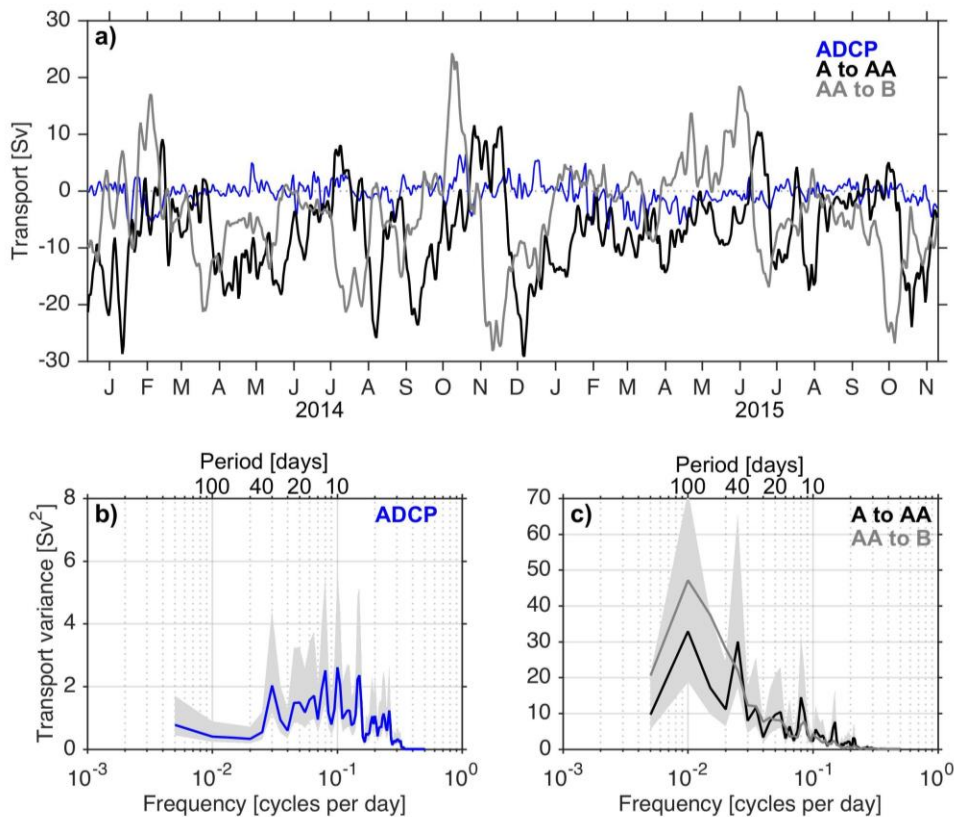
748           The meridional velocity measurements from the ADCP at the 411-m isobath on the  
749 upper slope (Figure 1, Table 1) provide useful insights about the flow variability and its spectral  
750 distribution up on the shelf inshore of Site A. If we assume the moored ADCP velocities are  
751 representative of the mean flow inshore of Site A (i.e., from the coast to the 1360 m isobath) and  
752 integrate them over this domain we obtain a mean and standard deviation of  $-0.4 \pm 2.0$  Sv for  
753 the 72-h low-pass filtered record (blue line in Figure 7a). The calculated transport from the  
754 ADCP velocities is very small compared to the absolute geostrophic transport estimates in the  
755 upper 628 dbar from the PIES/CPIES between Sites A and AA and between Sites AA and B  
756 (black and gray lines, respectively, in Figure 7a). The mean moored ADCP transport value also  
757 yields much smaller southward flow than the  $-2.7$  Sv determined as the average of the CTD  
758 snapshot sections (section 2.2.1), furthermore randomly subsampling the ADCP velocity profiles  
759 in a way that mimics the 4 CTD section snapshot realizations for 1000 iterations indicates that  
760 only a very low fraction of the random subsamples (about 7%) would produce a mean that is  
761 comparable to the CTD time mean of  $-2.7$  Sv. However, the mean moored ADCP transport  
762 compares well with the time-mean  $\sim -0.4$  to  $0.3$  Sv seasonally reversing flow at the shallow wide  
763 shelf from models (Palma et al., 2008). Additionally, while it is difficult to know for certain how  
764 representative the moored ADCP velocity is for the region inshore of Site A, we can definitely  
765 note that the largest portion of the variance (70%) in the ADCP record is associated with periods  
766 shorter than 40 days (Figure 7b; the spectra is calculated via Welch's periodogram method using  
767 a 200-day-wide Hamming window allowing 100 days of overlap), which seems likely to be  
768 unrelated to the BC transport variability, as the latter has a very prominent spectral peak near 100  
769 days (Figure 6a).

770           The ADCP record is short and perhaps a longer record would be able to reveal more  
771 pronounced variability on time scales longer than 40 days. However, we note that spectra of the  
772 BC transport records between Sites A-AA and AA-B for the identical time period as the ADCP  
773 record, 2014-2015 (Figure 7c), are able to show a clear peak at 100 days suggesting that different  
774 dynamics are governing the flow at the shelf/upper continental slope and in the BC region.

775           Given the roughly six-year length of our *in situ* transport records, estimates of the  
776 seasonal cycle and/or interannual variations can be made, with the understanding that the number  
777 of degrees of freedom is quite small. The annual climatology (average of each transport as a  
778 function of year day) of the observed 30-day low-pass filtered absolute transport from SAMBA-

779 West does not indicate a clear annual cycle for the period 2009-2015 for the absolute, baroclinic  
 780 or barotropic components (Figure 8). The absolute and baroclinic transports exhibit very similar  
 781 characteristics and amplitudes (Figure 8a, b), while the amplitude for the barotropic transport is  
 782 much smaller (Figure 8c).

783



784

785

786 **Figure 7.** Transport variability on the upper continental slope. a) Estimated 72-h low-pass  
 787 filtered transport from the ADCP deployed at the 411-m isobath integrated over the area inshore  
 788 of Site A (blue). Also shown are the 72-h low-pass filtered PIES/CPIES-derived absolute  
 789 geostrophic transports between Sites A and AA (black) and between Sites AA and B (gray)  
 790 during 2014-2015 when the ADCP and CPIES at Site AA measurements overlapped. b) Variance  
 791 preserving spectrum of daily 72-h low-pass filtered ADCP-derived transport. Shaded confidence  
 792 interval (95%) is also shown. c) Variance preserving spectrum of 72-h low-pass filtered  
 793 PIES/CPIES-derived absolute geostrophic transports between Sites A and AA (black) and  
 794 between Sites AA and B (gray; shaded confidence interval is not shown for clarity) during 2014-



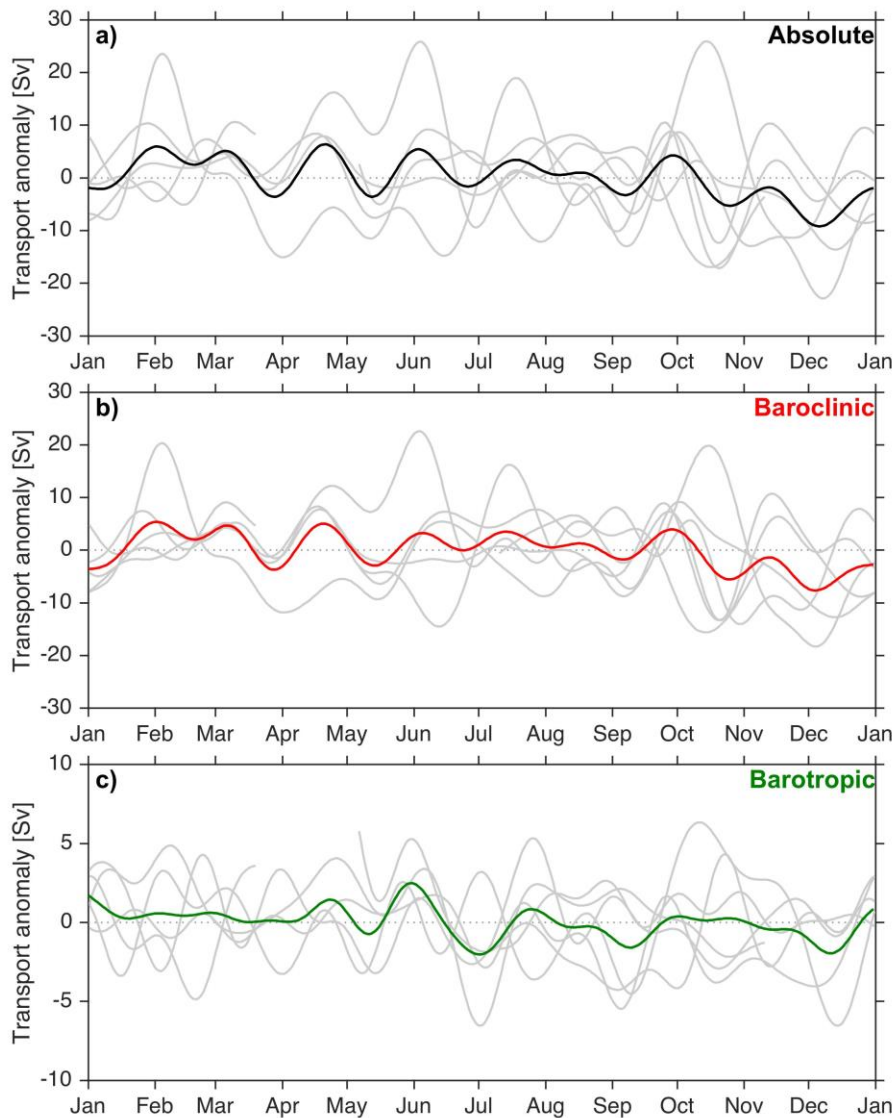
795 2015. Note the different scale on the y-axes for b) and c). The spectra are computed based on  
796 Welch's periodogram method using 200-days-wide Hamming window and 100-days of overlap  
797 between consecutive data segments.  
798

799 Our measurements show the strongest southward flow anomalies towards the end of the year in  
800 November-December, and the weakest southward flow anomalies during the first half of the  
801 year. Given the large high-frequency variability of the geostrophic component of the BC  
802 transport, its seasonality does not emerge from 6 years of continuous-in-time data – note the  
803 strong northward flow anomaly in October 2014 (strong anomaly in gray line in Figure 8a, b, c;  
804 see also Figure 5 and Table 4) when the seasonal cycle is shifting toward stronger southward  
805 transport anomalies (black and red curves in Figure 8a, b). The main difference among the three  
806 records occurs during January and July. During January, the three records have small amplitudes  
807 however both the absolute and baroclinic transport exhibit southward flow anomalies while the  
808 barotropic transport exhibits northward flow anomalies. For the period centered at the beginning  
809 of July the barotropic transport exhibits its largest southward flow anomalies, while the  
810 baroclinic transport have near zero or northward flow anomalies. If we estimate the seasonal  
811 cycle instead as monthly means, we similarly find no clear seasonal signal, with monthly values  
812 in the absolute transport anomalies that are not statistically different from zero or from each  
813 other at even the 67% confidence level (not shown). The seasonal cycle of the BC has previously  
814 been analyzed using XBTs (Dong et al. 2014; Goes et al. 2019), as well as with synthetic  
815 products derived from Argo data, satellite altimetry, winds, and with numerical models (e.g.,  
816 Matano, 1993; Combes & Matano, 2014; Schmid & Majumder, 2018). These studies  
817 consistently found a seasonal cycle with the BC intensifying during austral summer (January,  
818 February, March) and weakening during austral winter (June, July, August) at 35°S, consistent  
819 with the meridional displacements of the BMC at seasonal time scales (Olson et al. 1988; Goni  
820 & Wainer, 2001; Garzoli & Bianchi 1987; Garzoli & Garrafo, 1989; Saraceno et al., 2004;  
821 Lumpkin & Garzoli, 2011) associated with the seasonal variability of the basin-wide wind stress  
822 curl (e.g., Matano et al., 1993) or with the first mode of variability of the wind stress curl in a  
823 smaller domain in the western South Atlantic (Combes & Matano, 2014). However, we find that  
824 the directly locally-forced Ekman transport in the BC region at 34.5°S is very weak, and it has a  
825 very small temporal mean and standard deviation of  $-0.002 \pm 0.225$  Sv during 2009-2015 (not

826 shown). As in previous studies the Ekman transport anomaly has a well-defined seasonal cycle at  
827 this latitude, which reaches its maximum (positive) transport in austral winter and reaches its  
828 minimum (negative) transport in austral summer (e.g., Dong et al., 2014). Thus, the Ekman  
829 component of the BC transport (computed for the BC region) has a clear seasonality, but it is  
830 very weak (peak-to-peak amplitude of only  $\sim 0.16$  Sv) compared to the much larger monthly  
831 peak-to-peak BC geostrophic transport amplitude of  $\sim 9$  Sv. The standard deviation of the Ekman  
832 transport (of  $\pm 0.225$  Sv) is well below the scale of the standard deviation of the observed  
833 absolute or baroclinic transport signals (of 8.8 and 7.6 Sv, respectively) indicating that the  
834 observed geostrophic transport fluctuations cannot be caused by locally-forced changes induced  
835 by wind stress variability at any time scale. As a result, the annual climatology of the geostrophic  
836 absolute or baroclinic transports with the addition of the Ekman transport component yield  
837 similar results as in Figure 8a and 8b, respectively (not shown). Furthermore, there is a good  
838 correspondence between the calculated annual cycle of the BC and the DWBC below (Meinen et  
839 al., 2017), which is perhaps not surprising given the low shear between the two southward flows  
840 (e.g., Figure 4e). However, neither the BC or the DWBC show a meaningful annual cycle signal,  
841 possibly as a result of the aliasing of much stronger amplitude high frequency “noise” when  
842 attempting to extract the seasonal cycle. These results, combined with the low percent variance  
843 of absolute BC transport signals with periods longer than 150 days in Table 4, reveal that it is  
844 likely that more years of continuous measurements are needed to determine whether a robust  
845 seasonal cycle exists.

846 The annual means of the transport records for each individual year are given in Table 3.  
847 Note that years 2010 and 2011 have only three months and six months of data, respectively, and  
848 hence are excluded from this analysis. Years 2009 and 2015 have eight and ten months of data,  
849 respectively, and were judged usable for this analyses. During years 2009, 2012, and 2013, the  
850 annual mean absolute transport is markedly steady with only small variations compared to the  
851 record-length time-mean value of -14.0 Sv (-14.0, -14.7, and -14.8 Sv, respectively). During  
852 2014 the strongest southward flow is observed (-16.2 Sv) and during 2015 the weakest  
853 southward flow is observed (-10.8 Sv), differing from the time-mean by -2.2 Sv (stronger  
854 southward flow, due to enhanced southward baroclinic transport, Table 3) and 3.2 Sv (weaker  
855 southward flow, due to weaker baroclinic and barotropic transport, Table 3), respectively.  
856 However, the 95% confidence limits of the annual means calculated as  $2 \times \text{SEM}$  for each year-

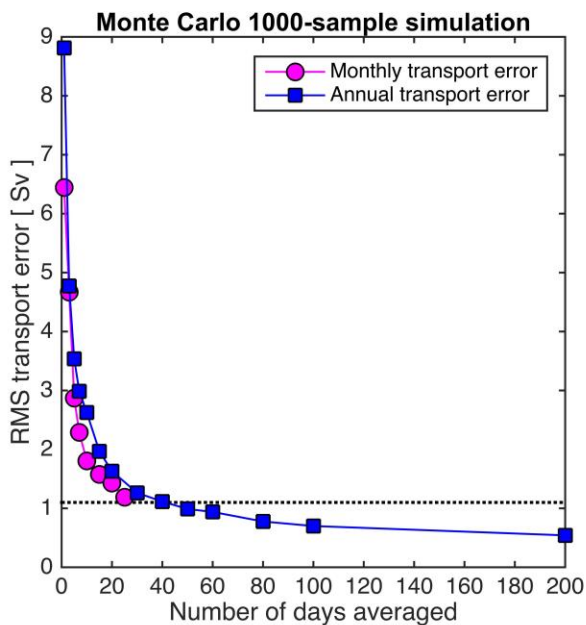
857 long segment are large (SEM is  $\sim 3.0$  Sv in 2014 and 2015). Additionally, fitting a linear  
 858 temporal trend to the absolute BC transport for the longest continuous segment (2011-2015)  
 859 yields  $0.08 \pm 1.78$  Sv/year ( $-0.05 \pm 1.52$  Sv/year and  $0.13 \pm 0.57$  Sv/year for the baroclinic and  
 860 barotropic transports, respectively), not statistically significant with 95% confidence for 64  
 861 DOFs following the methods of Bendat and Piersol (1986). Thus, there is no statistically  
 862 significant trend or deviations from the long-term mean in the yearly averages between 2009 and  
 863 2015.



864  
 865 **Figure 8.** Annual climatology (average for each year day) of 30-day low-pass filtered a)  
 866 absolute, b) baroclinic, and c) barotropic Brazil Current transport anomalies. Transport  
 867 anomalies are computed relative to the record-length mean. Light gray lines represent transport

868 anomalies for each individual year; the thick black, red and green lines are the temporal averages  
 869 of all individual years in a), b, and c) respectively. Note the different scale on the y-axes for c).  
 870 Negative values indicate southward flow anomaly.

871 To investigate the accuracy to which the monthly means and annual means can be  
 872 estimated from the available 6+ years long BC transport record, we estimate the errors in  
 873 monthly and annual means performing a Monte Carlo-style analysis (e.g., Emery and Thomson,  
 874 2001; Meinen et al. 2010). For the monthly averaging, we randomly selected a month from the  
 875 transport time series and then we randomly subsampled estimates of daily observations within  
 876 that chosen month. Subsamples ranging from one to twenty days were averaged and the root-  
 877 mean-square (RMS) error was computed between those averages and the average from the  
 878 complete month. A similar procedure is applied to obtain the RMS error of the annual mean  
 879 estimates. The results for 1000 iterations (Figure 9) indicate that, to consistently obtain a  
 880 monthly value accurate to within one SEM (of 1.1 Sv, Appendix A) at least 25 daily observations  
 881 within that month are needed. In order to obtain an annual mean value accurate to 1.1 Sv (or  
 882 better), at least 50 randomly sub-sampled daily observations are required during that year. These  
 883 results again point to the need of continuous-in-time daily measurements to resolve monthly to  
 884 interannual time scales in the BC transport.



885  
 886 **Figure 9.** Root-mean-square (RMS) error in the estimates of monthly (magenta) and annual  
 887 (blue) mean absolute Brazil Current transport versus number of samples considered, after a

888 Monte Carlo-style analysis with 1000 iterations. The horizontal dotted line indicates the Standard  
889 Error of the Mean (SEM) for the absolute transport record (1.1 Sv; Appendix A).

890

#### 891 **4 Summary and Conclusions**

892 The absolute Brazil Current (BC) transport at 34.5°S, integrated between the sea-surface  
893 and the mean-pressure of the density interface between TW/SACW and AAIW, during 2009-  
894 2015 has a mean strength of -14.0 Sv, a large standard deviation of 8.8 Sv, and a large peak-to-  
895 peak range of 61.7 Sv. Transport variations of 20-30 Sv occur in periods as short as 2-3 weeks  
896 and larger variations of about 40-60 Sv occur in periods of 30-60 days, illustrating the dynamic  
897 short-term variability in the record and the necessity of continuous-in-time daily observations to  
898 avoid aliasing. The daily transport values for the BC are estimated to be accurate to within 2.8 Sv  
899 (Appendix A). The long-term PIES/CPIES array at 34.5°S has been shown to capture the  
900 majority of the variability of the BC, centered mainly in the area between 51.5°W and 49.5°W.  
901 High-resolution hydrographic section data have been used to estimate the mean related transports  
902 near the shelf/shelf-break to the west of 51.5°W (which are not currently sampled by the  
903 PIES/CPIES array) and data from a bottom moored ADCP provided important insights about  
904 upper slope and shelf velocities. Our results indicate that additional time series observations at  
905 the shelf-break between the 500 and 1000 dbar isobaths would improve the overall estimation of  
906 the BC transport by the array. A new CPIES was deployed in mid 2019 west of PIES A at 875 m  
907 (Site 0A) and funding has been awarded to deploy a tall dynamic height mooring additionally  
908 equipped with current meters and biogeochemical sensors at the western boundary wedge  
909 currently not sampled by the PIES/CPIES array.

910 The results presented here reveal that the largest part of the variance (~80%) in the  
911 absolute BC transport is concentrated at periods shorter than 150 days. The spectral distribution  
912 of energy has a well-defined peak near 100 days and secondary (and noisier) peaks between 20-  
913 50 days, consistent with earlier studies of the DWBC at this same location (e.g., Meinen et al.,  
914 2017). The baroclinic component of the BC transport accounts for the largest fraction of the  
915 absolute transport variance (85%), but the barotropic variance contribution (15%) is not  
916 negligible. The baroclinic and barotropic transports are uncorrelated on a daily basis, and are  
917 only marginally correlated after smoothing with a 30-day low-pass filter. This highlights the  
918 need to measure both transport components independently in order to accurately describe the

919 flow variability. No statistically significant seasonal cycle is found and there is no statistically  
 920 significant trend or variability in the annual averages during the 6+ years of measurements. Our  
 921 analyses demonstrate that to consistently obtain a monthly value accurate to within 1.1 Sv (one  
 922 standard error level) at least 25 daily observations within that month are needed, and at least 50  
 923 randomly sub-sampled observations throughout a year are required to obtain an annual mean  
 924 value accurate to 1.1 Sv (or better). It is likely that more years of measurements are necessary to  
 925 clearly detect significant longer period (seasonal to interannual) signals and trends given the  
 926 large amplitude of the variability on short time scales.

927 Overall, the results presented here strongly highlight the strength of a continuous  
 928 observing system to capture the variability of the BC transport at subseasonal, seasonal, and  
 929 interannual time scales. A future study will address the physical mechanisms that drive the  
 930 meridional volume transport fluctuations observed here.

931

## 932 **Appendix A. Error analysis**

### 933 *Transport Accuracy Estimates*

934 The transport accuracy estimates closely follow the methods in Meinen et al. (2013). The  
 935 sources of the transport errors are classified as random or potential bias respective to the time  
 936 variability. A detailed explanation of the sources of each error is given in Meinen et al. (2013),  
 937 here we focus on the specifics of the BC estimate.

938 There are several sources of uncertainty that affect the  $\tau$  accuracy estimated from  
 939 PIES/CPIES. To convert the  $\tau$  accuracies into transport accuracies, we use the linear relationship  
 940 between the baroclinic streamfunction (a.k.a. Fofonoff potential or potential energy anomaly,  $\chi$ )  
 941 and  $\tau$  at 1000 dbar ( $\tau_{1000}$ ). Here the vertical integration domain for  $\chi$  is chosen to be consistent  
 942 with the layer occupied by the BC (ie. between the surface and approximately 628 dbar,  $\chi^{0-628}$ ).  
 943 There is a tight relationship between  $\tau$  and  $\chi^{0-628}$ . The slope for a linear fit is  $-0.6 \cdot 10^5 \text{ J m}^{-2} \text{ ms}^{-1}$ .  
 944 The  $\chi$  accuracy is converted into a transport error bars by using the local Coriolis parameter  $f = -$   
 945  $8.2605 \cdot 10^{-5} \text{ s}^{-1}$  and a constant density of  $1030 \text{ kg m}^{-3}$ .

946 The random sources of the geostrophic velocity or transport (baroclinic relative to an  
 947 assumed level of no motion and barotropic or reference velocity) affect the time-variability of the  
 948 transport and can be listed as follows: 1) the accuracy of PIES/CPIES-measured  $\tau$  (0.17 ms;

949 following Chidichimo et al., 2014, revised after Donohue et al., 2010); 2) the scatter in the  
950 calibration relationship to convert PIES/CPIES  $\tau$  actual depth on the fixed 1000 dbar level (0.2  
951 ms or 0.5 Sv; as estimated in Meinen et al., 2013); 3) the accuracy of the GEM lookup tables  
952 calculated as the rms scatter about the fit between  $\chi^{0-628}$  and  $\tau_{1000}$  ( $1.65 \times 10^5 \text{ J m}^{-2}$ ); 4)  
953 additionally, for the calculation of the reference velocity accuracy the sole random source of  
954 error are the pressure gauges (0.01 dbar; Donohue et al., 2010). These four random errors  
955 amount to 1.9, 0.5, 1.8, and 0.7 Sv, respectively (independent of one another) and are combined  
956 via the square-root of the sum of the squares method yielding a total random error of 2.8 Sv for  
957 the 72-h low-pass filtered BC transport estimates.

958 There are two potential sources bias errors affecting the time-mean transport: 1) the offset  
959 due to the calibration of  $\tau$  into the equivalent  $\tau_{\text{index}}$  from CTDs (1.8 ms or 1.9 Sv from Meinen et  
960 al., 2013); 2) the accuracy of the time-mean reference velocity between Sites A and B, estimated  
961 conservatively as the difference of time-mean reference velocity at 1500 dbar between two  
962 sources: the 35-year run of OFES (1980-2015) described herein ( $-0.058 \text{ m s}^{-1}$ ) and a 26-year run  
963 (1992-2018) of the Estimating the Circulation and Climate of the Ocean, Phase 2 (ECCO2)  
964 ocean state estimate (<https://ecco.jpl.nasa.gov/>) ( $-0.027 \text{ m s}^{-1}$ ). The approximate difference  
965 between these estimates amount to  $0.031 \text{ m s}^{-1}$ , which considering a width of  $1.8315 \times 10^5 \text{ m}$  and  
966 a vertical layer of about 628 m translates into a potential transport bias error of 3.5 Sv. Adding  
967 more models would refine/reduce the estimate of this source of bias in the future, but this is  
968 beyond the scope of this study. As these potential bias sources of errors are independent of one  
969 another, they are also combined via the square-root of the sum of the squares, yielding 3.9 Sv.  
970

#### 971 *Degrees of freedom, integral time scales, standard error of the mean*

972 The integral time scale (ITS) for the absolute transport record is determined by the first  
973 zero crossing of the autocorrelation function of the daily transport time series (Emery and  
974 Thomson, 2001). Evaluating the longest segment with continuous measurements (between July  
975 2011 and November 2015, almost 4.5 years of data) of the absolute transport record, results in an  
976 ITS of 12 days, thus every 24 days there is an independent “degree of freedom” (DOF) for  
977 estimating both the average and the statistical accuracy of the average. This yields about 64  
978 DOFs and a Standard Error of the Mean (SEM) of 1.1 Sv. If we also include the first one-year  
979 segment in the analysis, the DOFs increase to 76 and the resulting SEM is 1.0 Sv. To be

980 conservative we keep the estimate for the longest period with continuous measurements. The ITS  
981 after applying a 30-day low-pass filter is slightly longer (14 days), thus the time series have  
982 fewer DOFs (56). The statistical significance of the correlation coefficients is calculated  
983 following the methodology described in Emery and Thomson (2001). For 60 DOFs, correlations  
984 ( $r$ ) for 72-h low pass filtered records with cutoff  $r = |0.250|$  and  $r = |0.325|$  are significantly  
985 different from zero at the 95% and the 99% confidence level, respectively. For 50 DOFs,  
986 correlations with cutoff  $r = |0.273|$  and  $r = |0.354|$  are significantly different from zero at the 95%  
987 and the 99% confidence level, respectively.

988

### 989 **Acknowledgements**

990 The authors would like to thank the crews of Puerto Deseado and Ice Lady Patagonia II  
991 (Argentina), Alpha-Crucis, Alpha-Delphini and Cruzeiro do Sul (Brazil), who have supported the  
992 research cruises. Thanks also to the support/technical teams in Miami, São Paulo, Buenos Aires,  
993 who have helped collect and process the data presented herein. M. Charo, R. Guerrero, D. Valla,  
994 C. França, R. Garcia, P. Peña, and U. Rivero are gratefully acknowledged for their invaluable  
995 work with the collection and calibration of the hydrographic and PIES data used in this study.  
996 The SAMBA-West hydrographic observations and the participation of MPC and AP were  
997 supported by funds from Servicio de Hidrografía Naval, CONICET, NOAA, and the Inter-  
998 American Institute for Global Change Research grants CRN2076 and CRN3070, through the U.  
999 S. National Science Foundation grants GEO-0452325 and GEO-1128040. The U.S. PIES  
1000 observations and the participation of CM, RP, SD, and SG were supported via the NOAA Global  
1001 Ocean Monitoring and Observing program (FundRef# 100007298) under the Southwest Atlantic  
1002 Meridional Overturning Circulation (“SAM”) project. The Brazilian CPIES and ADCP  
1003 observations and the participation of EC were supported by CNPq (Grant 302503/2019-6) and  
1004 FAPESP through projects SAMOC (Grant 2011/50552-4) and SAMBAR (Grant 2017/09659-6).  
1005 MPC and AP also acknowledge funding support from the European Union’s Horizon 2020  
1006 Research and Innovation Programme under grant agreement no. 818123 (iAtlantic). CM, RP,  
1007 SD, RL, SG also acknowledge additional support from the NOAA Atlantic Oceanographic and  
1008 Meteorological Laboratory. CM and RP acknowledge additional support from NOAA Climate  
1009 Variability Program (GC16-212). RP and SG acknowledge additional support from NOAA  
1010 (grant NA13OAR4310131) and NASA (grant NNX14AH60G). SD acknowledge additional



1011 support from NOAA Climate Variability Program (GC16-210) and NOAA Global Ocean  
1012 Monitoring and Observing program under the XBT project and State of the Climate: Quarterly  
1013 Report on the Meridional Heat Transport in the Atlantic Ocean project. Thanks to D. Volkov for  
1014 providing the run from the Estimating the Circulation and Climate of the Ocean, Phase 2  
1015 (ECCO2) ocean state estimate (<https://ecco.jpl.nasa.gov/>). We are very grateful for the  
1016 constructive comments by two anonymous reviewers.

1017  
1018 **Data:** The PIES/CPIES and hydrographic data used herein from the South Atlantic MOC Basin-  
1019 wide Array (SAMBA) can be found at:  
1020 [https://www.aoml.noaa.gov/phod/SAMOC\\_international/samoc\\_data.php](https://www.aoml.noaa.gov/phod/SAMOC_international/samoc_data.php)  
1021 The STSF hydrographic and LADCP data are available at <https://doi.org/10.7910/DVN/IHWLL3>  
1022 and <https://doi.org/10.7910/DVN/JJNFKG>, respectively.

1023

## 1024 **References**

1025 Ansorge, I. J., Baringer, M. O., Campos, E. J. D., Dong, S., Fine, R. A., Garzoli, S. L., et  
1026 al. (2014). Basin-wide oceanographic array bridges the South Atlantic. *Eos Transactions,*  
1027 *American Geophysical Union*, 95(6), 53–54, doi:10.1002/2014EO060001.

1028 Archer, M. R., Keating, S. R., Roughan, M., Johns, W. E., Lumpkin, R., Beron-Vera, F.  
1029 J., & Shay, L. K. (2018). The kinematic similarity of two western boundary currents revealed by  
1030 sustained high-resolution observations. *Geophysical Research Letters*, 45.  
1031 <https://doi.org/10.1029/2018GL078429>

1032 Bendat, J. S. & Piersol, A. G. (1986). *Random data: Analysis and measurement*  
1033 *procedures* (2nd Edition). Wiley Interscience, New York, 566pp.

1034 Berden, G., Charo, M., Möller, O. O., & Piola, A. R. (2020). Circulation and  
1035 hydrography in the western south atlantic shelf and export to the deep adjacent ocean: 30°S to  
1036 40°S. *Journal of Geophysical Research: Oceans*, 125, e2020JC016500.  
1037 <https://doi.org/10.1029/2020JC016500>

1038 Bianchi A. A., & Garzoli, S. L. (1997). Variability and motion of the Brazil-Malvinas  
1039 front. *GEOACTA*, 22, 74-90.

- 1040 Biastoch, A., Böning, C. W., & Lutjeharms, J. R. E. (2008). Agulhas leakage dynamics  
1041 affects decadal variability in atlantic overturning circulation, *Nature Geoscience*, 456, 489–492,  
1042 doi:10.1038/nature07426.
- 1043 Biló, T. C., da Silveira, I. C. A., Belo, W. C., de Castro, B. M., & Piola, A. R. (2014).  
1044 Methods for estimating the velocities of the Brazil Current in the pre-salt reservoir area off  
1045 southeast Brazil (23°S–26°S). *Ocean Dynamics*, 64(10), 1431–1446, doi: 10.1007/s10236-014-  
1046 0761-2.
- 1047 Bishop, S. P., Watts, D. R., Park, J. -H., & Hogg, N. G. (2012). Evidence of bottom-  
1048 trapped currents in the Kuroshio Extension region. *Journal of Physical Oceanography*,  
1049 42(2):321–328. (doi:10.1175/JPO-D-11-0144.1)
- 1050 Boebel, O., Davis, R. E., Ollittraut, M., Peterson, R. G., Richard, P. L., Schmid, C., &  
1051 Zenk, W. (1999). The intermediate depth circulation of the western South Atlantic. *Geophysical*  
1052 *Research Letters*, 26, 3329–3332. <https://doi.org/10.1029/1999GL002355>
- 1053 Bryden, H. L., King, B.A. & McCarthy, G. D. (2011). South Atlantic overturning  
1054 circulation at 24°S. *Journal of Marine Research*, 69 (1), 38-56.  
1055 ([doi:10.1357/002224011798147633](https://doi.org/10.1357/002224011798147633)).
- 1056 Buckley, M. W., & J. Marshall (2016). Observations, inferences, and mechanisms of the  
1057 atlantic meridional overturning circulation: A review. *Reviews of Geophysics*, 54(1), 5–63,  
1058 doi:10.1002/2015RG000493, 2015RG000493.
- 1059 Calado, L., Da Silveira, I.C.A., Gangopadhyay, A. & De Castro, B.M. (2010). Eddy-  
1060 induced upwelling off Cape São Tomé (22°S, Brazil). *Continental Shelf Research*, 30 (10-11),  
1061 pp.1181-1188. <https://doi.org/10.1016/j.csr.2010.03.007>
- 1062 Campos, E. J. D., Gonçalves, J. E., & Ikeda, Y. (1995). Water mass characteristics and  
1063 geostrophic circulation in the South Brazil Bight: Summer of 1991. *Journal of Geophysical*  
1064 *Research*, 100(C9), 18537– 18550, doi:10.1029/95JC01724.
- 1065 Campos, E.J., Velhote, D., & da Silveira, I. C. (2000). Shelf break upwelling driven by  
1066 Brazil Current cyclonic meanders. *Geophysical Research Letters*, 27(6), pp.751-754.  
1067 <https://doi.org/10.1029/1999GL010502>
- 1068 Charo, M., Guerrero, R., & Piola, A. (2020a). "Subtropical Shelf Front cruise -  
1069 Conductivity-Temperature-Depth (CTD) data", <https://doi.org/10.7910/DVN/IHWLL3>, Harvard  
1070 Dataverse, V1.

- 1071 Charo, M., Valla, D., Fenco, H., & Piola, A. (2020b). "Subtropical Shelf Front cruise -  
1072 Lowered Acoustic Doppler Profiler (LADCP) data", <https://doi.org/10.7910/DVN/JJNFKG>,  
1073 Harvard Dataverse, V1.
- 1074 Chidichimo, M. P., Donohue, K. A., Watts, D. R., & Tracey, K. L. (2014). Baroclinic  
1075 transport time series of the Antarctic Circumpolar Current measured in Drake Passage. *Journal of*  
1076 *Physical Oceanography*, 44(7), 1829–1853, doi:10.1175/JPO-D-13-071.1.
- 1077 Confluence Principal Investigators (1990). CONFLUENCE 1988-1990: An intensive  
1078 study of the southwestern Atlantic, *Eos Trans. AGU*, 71(41), 1131–1133,  
1079 doi: 10.1029/90EO00313.
- 1080 Combes, V., & Matano, R. (2014). A two-way nested simulation of the oceanic  
1081 circulation in the Southwestern Atlantic. *Journal of Geophysical Research: Oceans*, 119(2), 731–  
1082 756, doi:10.1002/2013JC009498.
- 1083 Côté, J. M., Hotchkiss, F. S., Martini, M., & Denham, C. R. (2011). Acoustic Doppler  
1084 Current Profiler (ADCP) data processing system manual: U.S. Geological Survey Open File  
1085 Report 00-458, v. 4, 51 p.
- 1086 de Souza, M.M., Mathis, M., & Pohlmann, T. (2019). Driving mechanisms of the  
1087 variability and long-term trend of the Brazil–Malvinas confluence during the 21st century.  
1088 *Climate Dynamics*, 53, 6453–6468. <https://doi.org/10.1007/s00382-019-04942-7>
- 1089 Dong, S., Garzoli, S. L., Baringer, M. O., Meinen, C. S., & Goni, G. J. (2009). The  
1090 Atlantic Meridional Overturning Circulation and its Northward Heat Transport in the South  
1091 Atlantic. *Geophysical Research Letters*, 36, L20606, doi:10.1029/2009GL039356.
- 1092 Dong, S., Baringer, M., Goni, G. & Garzoli, S. (2011a). Importance of the assimilation of  
1093 Argo Float Measurements on the Meridional Overturning Circulation in the South Atlantic.  
1094 *Geophysical Research Letters*, 38, L18603, doi:10.1029/2011GL048982.
- 1095 Dong, S., Baringer, M. O., Goni, G. J., Meinen, C. S., & Garzoli, S. L. (2014). Seasonal  
1096 variations in the South Atlantic Meridional Overturning Circulation from observations and  
1097 numerical models. *Geophysical Research Letters*, 41, doi:10.1002/2014GL060428.
- 1098 Dong, S., G. Goni G., & Bringas, F. (2015). Temporal variability of the Meridional  
1099 Overturning Circulation in the South Atlantic between 20°S and 35°S. *Geophysical Research*  
1100 *Letters*, 42, 7655 - 7662, (doi:10.1002/2015GL065603).

- 1101 Donohue, K. A., Watts, D. R., Tracey, K. L., Greene, A. D., & Kenelly, M. (2010).  
1102 Mapping circulation in the Kuroshio Extension with an array of current and pressure recording  
1103 inverted echo sounders. *Journal of Atmospheric and Oceanic Technology*, 27, 507–527.  
1104 <https://doi.org/10.1175/2009JTECHO686.1>
- 1105 Drouin, K. L., Lozier, M. S., & Johns, W. E. (2021). Variability and trends of the South  
1106 Atlantic subtropical gyre. *Journal of Geophysical Research: Oceans*. doi:10.1029/2020jc016405
- 1107 Emery, W. J., & Thomson, R. E. (2001). *Data Analysis Methods in Physical*  
1108 *Oceanography*, edited by W. J. Emery and R. E. Thomson, pp. 654, Elsevier Science,  
1109 Amsterdam, doi: <https://doi.org/10.1016/B978-0-444-50756-3.X5000-X>.
- 1110 Ferrari, R., Artana, C., Saraceno, M., Piola, A. R., & Provost, C. (2017). Satellite  
1111 altimetry and current- meter velocities in the Malvinas Current at 41°S: Comparisons and modes  
1112 of variations. *Journal of Geophysical Research: Oceans*, 122, 9572– 9590.  
1113 <https://doi.org/10.1002/2017JC013340>
- 1114 Frajka-Williams, E., Anson, I. J., Baehr, J., Bryden, H. L., Chidichimo, M. P.,  
1115 Cunningham, S.A., et al. (2019). Atlantic Meridional Overturning Circulation: Observed  
1116 transports and variability. *Frontiers in Marine Science*, 6:260, doi:10.3389/fmars.2019.00260.
- 1117 Garfield, N., III (1990), *The Brazil Current at subtropical latitudes*, Ph.D.thesis, 121 pp.,  
1118 Univ. of R. I., Kingston.
- 1119 Garzoli, S. L., and Bianchi, A. (1987). Time- space variability of the local dynamics of  
1120 the Malvinas- Brazil confluence as revealed by inverted echo sounders, *Journal of Geophysical*  
1121 *Research*. 92(C2), 1914– 1922, doi:10.1029/JC092iC02p01914.
- 1122 Garzoli S. L., & Garraffo, Z. (1989). Transports, frontal motions and eddies at the Brazil-  
1123 Malvinas currents confluence. *Deep Sea Research Part A. Oceanographic Research Papers*,  
1124 Volume 36, Issue 5, Pages 681-703, ISSN 0198-0149, [https://doi.org/10.1016/0198-](https://doi.org/10.1016/0198-0149(89)90145-3)  
1125 [0149\(89\)90145-3](https://doi.org/10.1016/0198-0149(89)90145-3).
- 1126 Garzoli, S. L., & Simionato, C. (1990). Baroclinic instabilities and forced oscillations in  
1127 the brazil/malvinas confluence front. *Deep Sea Research Part A. Oceanographic Research*  
1128 *Papers*, 37(6), 1053 – 1074, doi: [https://doi.org/10.1016/0198-0149\(90\)90110-H](https://doi.org/10.1016/0198-0149(90)90110-H).

- 1129 Garzoli, S. L. (1993). Geostrophic velocity and transport variability in the Brazil-  
 1130 Malvinas confluence. *Deep Sea Research Part I: Oceanographic Research Papers*, 40(7), 1379 –  
 1131 1403, doi:[http://dx.doi.org/10.1016/0967-0637\(93\)90118-M](http://dx.doi.org/10.1016/0967-0637(93)90118-M).
- 1132 Garzoli, S. L., & Baringer, M. O. (2007). Meridional heat transport determined with  
 1133 expandable bathythermographs Part II: South Atlantic transport. *Deep Sea Research Part I:*  
 1134 *Oceanographic Research*, 54, 1402–1420, doi:10.1016/j.dsr.2007.04.013.
- 1135 Garzoli, S. L., & Matano, R. (2011). The South Atlantic and the Atlantic Meridional  
 1136 Overturning Circulation. *Deep Sea Research Part II: Topical Studies in Oceanography*, 58(17-  
 1137 18), 1837 – 1847, doi: <https://doi.org/10.1016/j.dsr2.2010.10.063>.
- 1138 Garzoli, S., Abrahamsen, P., Ansorge, I., Biastoch, A., Campos, E., Mata, M. et al.  
 1139 (2012). South Atlantic Meridional Overturning Circulation (SAMOC) - Fourth Workshop,  
 1140 CLIVAR Exchanges, 58, 2-4.
- 1141 Garzoli, S. L., Baringer, M. O., Dong, S., Perez, R. C., & Yao, Q. (2013). South Atlantic  
 1142 meridional fluxes. *Deep Sea Research Part I: Oceanographic Research Papers*, 71, 21 – 32,  
 1143 doi:<http://dx.doi.org/10.1016/j.dsr.2012.09.003>.
- 1144 Gill, A. (1982), *Atmosphere-Ocean Dynamics*, 1st Edition, International Geophysics  
 1145 series, Volume 30, Academic Press, London, UK, p. 662. ISBN: 9780122835223.
- 1146 Goes, M., Goni, G., & Dong, S. (2015). An optimal XBT-based monitoring system for  
 1147 the South Atlantic Meridional Overturning Circulation at 34°S. *Journal of Geophysical Research*,  
 1148 120, 1161-1181, doi:10.1002/2014GL061802.
- 1149 Goni, G., Kamholz, S., Garzoli, S., & Olson, D. (1996). Dynamics of the Brazil-Malvinas  
 1150 Confluence based on inverted echo sounders and altimetry. *Journal of Geophysical Research:*  
 1151 *Oceans*, 101(C7), 16273–16289. doi:10.1029/96jc01146
- 1152 Goni, G. J., & Wainer, I. (2001). Investigation of the Brazil Current front variability from  
 1153 altimeter data. *Journal of Geophysical Research*, 106(C12), 31117– 31128,  
 1154 doi:[10.1029/2000JC000396](https://doi.org/10.1029/2000JC000396).
- 1155 Goni, G. J., Bringas, F., & DiNezio, P. N. (2011). Observed low frequency variability of  
 1156 the Brazil Current front. *Journal of Geophysical Research: Oceans*, 116(C10), n/a–n/a,  
 1157 doi:10.1029/2011JC007198, c10037.

- 1158 Gordon A. L., & Greengrove, C. L. (1986). Geostrophic circulation of the Brazil-  
1159 Falkland confluence. *Deep Sea Research Part A. Oceanographic Research Papers*, Volume 33,  
1160 Issue 5, Pages 573-585, [https://doi.org/10.1016/0198-0149\(86\)90054-3](https://doi.org/10.1016/0198-0149(86)90054-3).
- 1161 Herrford, J., Brandt, P., Kanzow, T., Hummels, R., Araujo, M., & Durgadoo, J. V.  
1162 (2021). Seasonal variability of the Atlantic Meridional Overturning Circulation at 11° S inferred  
1163 from bottom pressure measurements, *Ocean Sci.*, 17, 265–284, [https://doi.org/10.5194/os-17-](https://doi.org/10.5194/os-17-265-2021)  
1164 265-2021, 2021.
- 1165 Hummels, R., Brandt, P., Dengler, M., Fischer, J., Araujo, M., Veleda, D., & Durgadoo,  
1166 J. V. (2015). Interannual to decadal changes in the western boundary circulation in the Atlantic at  
1167 11°S. *Geophysical Research Letters*, 42, 7615– 7622, doi:[10.1002/2015GL065254](https://doi.org/10.1002/2015GL065254).
- 1168 Imawaki, S., Bower, A., Beal, L., & Qiu, B. (2013). “Western boundary currents,” in  
1169 *Ocean Circulation and Climate – a 21st Century Perspective*, eds G. Siedler, S. M. Griffies, J.  
1170 Gould, and J. A. Church (Amsterdam: Elsevier Academic Press), 305–338. doi: 10.1016/B978-0-  
1171 12-391851-2.00013-1
- 1172 Jackett, D. R., & McDougall, T. J. (1997). A Neutral Density Variable for the World’s  
1173 Oceans, *Journal of Physical Oceanography*, 27(2), 237-263. Retrieved Dec 28, 2020, from  
1174 [https://journals.ametsoc.org/view/journals/phoc/27/2/1520-](https://journals.ametsoc.org/view/journals/phoc/27/2/1520-0485_1997_027_0237_andvft_2.0.co_2.xml)  
1175 0485\_1997\_027\_0237\_andvft\_2.0.co\_2.xml
- 1176 Kersalé, M., Perez, R. C., Speich, S., Meinen, C. S., Lamont, T., Le Hénaff, M., et al.  
1177 (2019). Shallow and deep eastern boundary currents in the South Atlantic at 34.5°S: Mean  
1178 structure and variability. *Journal of Geophysical Research: Oceans*, 124, 1634– 1659, 1634–  
1179 1659. <https://doi.org/10.1029/2018JC014554>
- 1180 Kersalé, M., Meinen, C. S., Perez, R. C., Le Hénaff, M., Valla, D., Lamont, T., et al.  
1181 (2020). Highly Variable Upper and Abyssal Overturning Cells in the South Atlantic. *Science*  
1182 *Advances*, Vol. 6, no. 32, eaba7573, doi: 10.1126/sciadv.aba7573, 2020.
- 1183 King, B. A., & Hamersley, D. R. C. (2010). RRS James Cook cruise JC032, 07 March to  
1184 21 April 2009. Hydrographic sections across the Brazil Current and at 24°S in the Atlantic.  
1185 National Oceanographic Centre Southampton, Southampton, UK, 173.
- 1186 Lima, M. O., Cirano, M., Mata, M. M., Goes, M., Goni, G., & Baringer, M. O (2016).  
1187 An assessment of the Brazil Current baroclinic structure and variability near 22°S in distinct

1188 ocean forecasting and analysis systems. *Ocean Dynamics*, 66(6-7), 893–916,

1189 doi:10.1007/s10236-016-0959-6.

1190 Lumpkin, R., & Garzoli, S. (2011). Interannual to decadal changes in the western South

1191 Atlantic's surface circulation. *Journal of Geophysical Research: Oceans*, 116(C1), n/a– n/a,

1192 doi:10.1029/2010JC006285, c01014.

1193 Matano, R. P., Schlax, M. G., & Chelton, D. B. (1993). Seasonal variability in the

1194 southwestern Atlantic. *Journal of Geophysical Research*, 98(C10), 18027– 18035,

1195 doi:[10.1029/93JC01602](https://doi.org/10.1029/93JC01602).

1196 Meinen, C. S., & Watts, D. R. (2000). Vertical structure and transport on a transect across

1197 the North Atlantic Current near 42°N: Time series and mean. *Journal of Geophysical Research*,

1198 105, 869–891, doi:10.1029/2000JC900097.

1199 Meinen, C. S., Baringer, M. O., & Garcia, R. F. (2010). Florida Current transport

1200 variability: An analysis of annual and longer-period signals. *Deep Sea Research Part I:*

1201 *Oceanographic Research Papers*, Volume 57, Issue 7, Pages 835-846,ISSN 0967-0637,

1202 <https://doi.org/10.1016/j.dsr.2010.04.001>.

1203 Meinen, C. S., Piola, A. R., Perez, R. C., & Garzoli, S. L. (2012). Deep Western

1204 Boundary Current transport variability in the South Atlantic: preliminary results from a pilot

1205 array at 34.5°S. *Ocean Science*, 8(6), 1041–1054, doi:10.5194/os-8-1041-2012.

1206 Meinen, C. S., Speich, S., Perez, R. C., Dong, S., Piola, A. R., Garzoli, S. L., et al.

1207 (2013). Temporal variability of the meridional overturning circulation at 34.5°S: Results from

1208 two pilot boundary arrays in the South Atlantic. *Journal of Geophysical Research: Oceans*,

1209 118(12), 6461–6478, doi:10.1002/2013JC009228.

1210 Meinen, C. S., & Douglas S. L. (2016). Structure, transport, and vertical coherence of the

1211 Gulf Stream from the Straits of Florida to the Southeast Newfoundland Ridge. *Deep Sea*

1212 *Research Part I: Oceanographic Research Papers*, Volume 112, Pages 137-154,ISSN 0967-0637,

1213 <https://doi.org/10.1016/j.dsr.2016.03.002>.

1214 Meinen, C. S., Garzoli, S.L., Perez, R. C., Campos, E., Piola, A. R., Chidichimo, M. P., et

1215 al. (2017). Characteristics and causes of Deep Western Boundary Current transport variability at

1216 34.5°S during 2009–2014. *Ocean Science*, 13(1), 175–194, doi:10.5194/os-13-175-2017.

1217 Meinen, C. S., Speich, S., Piola, A. R., Ansong, I., Campos, E., Kersalé, M., et al.

1218 (2018). Meridional overturning circulation transport variability at 34.5°S during 2009-2017:

- 1219 Baroclinic and barotropic flows and the dueling influence of the boundaries. *Geophysical*  
1220 *Research Letters*, 45(9), 4180–4188, doi: 10.1029/2018GL077408, na.
- 1221 Müller, T. J., Ikeda, Y., Zangenberg, N., & Nonato, L. V. (1998). Direct measurements of  
1222 western boundary currents off Brazil between 20° and 28°S. *Journal of Geophysical Research:*  
1223 *Oceans*, 103(C3), 5429–5437, doi:10.1029/97JC03529.
- 1224 Munk, W., & Cartwright, D. (1996). Tidal spectroscopy and prediction. *Philosophical*  
1225 *Transactions of the Royal Society of London. Series A, Mathematical and Physical Sciences* 259  
1226 (1966): 533 - 581. <https://doi.org/10.1098/rsta.1966.0024>
- 1227 Oliveira, L. R., Piola, A. R., Mata, M. M., & Soares, I. D. (2009). Brazil Current surface  
1228 circulation and energetics observed from drifting buoys. *Journal of Geophysical Research*, 114,  
1229 C10006, doi:10.1029/2008JC004900.
- 1230 Olson, D. B., Podesta, G. P., Evans, R. H., & Brown, O. B. (1988). Temporal variations  
1231 in the separation of Brazil and Malvinas currents. *Deep Sea Research Part A, Oceanographic*  
1232 *Research Papers*, 35(12), 1971–1990, doi:10.1016/0198-0149(88)90120-3, na.
- 1233 Palma, E. D., Matano, R. P., & Piola, A. R. (2004). A numerical study of the  
1234 Southwestern Atlantic Shelf circulation: Barotropic response to tidal and wind forcing. *Journal*  
1235 *of Geophysical Research*, 109, C08014, doi:[10.1029/2004JC002315](https://doi.org/10.1029/2004JC002315).
- 1236 Palma, E. D., Matano, R. P., & Piola, A. R. (2008). A numerical study of the south-  
1237 western Atlantic shelf circulation: Stratified ocean response to local and offshore forcing. *Journal*  
1238 *of Geophysical Research: Oceans*, 113(C11), n/a–n/a, doi: 10.1029/2007JC004720, c11010.
- 1239 Palmer, M. D., Durack, P., Chidichimo, M. P., Church, J., Cravatte, S. E., Hill, K. L., et  
1240 al. (2019). Adequacy of the ocean observation system for quantifying regional heat and  
1241 freshwater storage and change. *Frontiers in Marine Science* 6:416. doi:  
1242 [10.3389/fmars.2019.00416](https://doi.org/10.3389/fmars.2019.00416)
- 1243 Perez, R. C., Garzoli, S. L., Meinen, C. S., & Matano, R. P. (2011). Geostrophic Velocity  
1244 Measurement Techniques for the Meridional Overturning Circulation and Meridional Heat  
1245 Transport in the South Atlantic. *Journal of Atmospheric and Oceanic Technology*, 28, 1504-  
1246 1521, doi:10.1175/JTECH-D-11-00058.1.
- 1247 Peterson, R. G., & Stramma, L. (1991). Upper-level circulation in the South Atlantic  
1248 ocean. *Progress in Oceanography*, 26, 1–73.



- 1249 Rennell, J. (1832). Investigation of the currents of the Atlantic Ocean, and of those which  
1250 prevail between the Indian Ocean and the Atlantic. London: Published for Lady Rodd by J.G. &  
1251 F. Rivington, (OCoLC)757616581, p. 359.
- 1252 Riser, S., Freeland, H., Roemmich, D. Wijffels, S., Troisi, A., Belbéoch, M., et al.  
1253 (2016). Fifteen years of ocean observations with the global Argo array. *Nature Climate*  
1254 *Change* 6, 145–153 (2016). <https://doi.org/10.1038/nclimate2872>.
- 1255 Rodrigues, R. R., Rothstein, L. M., & Wimbush, M. (2007). Seasonal variability of the  
1256 South Equatorial Current bifurcation in the Atlantic Ocean: A numerical study. *Journal of*  
1257 *Physical Oceanography*, 37(1), 16–30. <https://doi.org/10.1175/JPO2983.1>
- 1258 Rodrigues R. R., Wimbush M., Watts D. R., Rothstein L. M., & Ollitrault M. (2010).  
1259 South Atlantic mass transports obtained from subsurface float and hydrographic data *Journal of*  
1260 *Marine Research*. 68: 1216 819-850. doi: 10.1357/002224010796673858.
- 1261 Rossby, T. (1969). On monitoring depth variations of the main thermocline  
1262 acoustically, *Journal of Geophysical Research*, 74(23), 5542– 5546,  
1263 doi:[10.1029/JC074i023p05542](https://doi.org/10.1029/JC074i023p05542).
- 1264 Rühls, S., Getzlaff, K., Durgadoo, J. V., Biastoch, A., & Böning, C. W. (2015). On the  
1265 suitability of North Brazil Current transport estimates for monitoring basin-scale AMOC  
1266 changes. *Geophysical Research Letters*, 42, 8072–8080, doi:10.1002/2015GL065695.
- 1267 Saraceno, M., Provost, C., Piola, A. R., Bava, J., & Gagliardini, A. (2004). Brazil  
1268 Malvinas Frontal System as seen from 9 years of advanced very high resolution radiometer data.  
1269 *Journal of Geophysical Research*, 109, C05027, doi:[10.1029/2003JC002127](https://doi.org/10.1029/2003JC002127).
- 1270 Sasaki, H., Nonaka, M., Masumoto, Y., Sasai, Y., Uehara, H., & Sakuma, H. (2008). An  
1271 eddy-resolving hindcast simulation of the quasiglobal ocean from 1950 to 2003 on the Earth  
1272 Simulator. In *High resolution numerical modelling of the atmosphere and ocean*, pp. 157-185,  
1273 Springer, New York, NY.
- 1274 Schmid, C. (2014): Mean vertical and horizontal structure of the subtropical circulation in  
1275 the South Atlantic from three-dimensional observed velocity fields. *Deep Sea Research I*, 91 (9),  
1276 50-71, doi: 10.1016/j.dsr.2014.04.015.
- 1277 Schmid, C., & Majumder, S. (2018). Transport variability of the Brazil Current from  
1278 observations and a data assimilation model. *Ocean Science*, 14(3), 417–436, doi: 10.5194/os-14-  
1279 417-2018.

- 1280 Smith, W. H. F., & Sandwell, D. T. (1997). Global seafloor topography from satellite  
1281 altimetry and ship depth soundings, *Science*, 277, 1957–1962. DOI:  
1282 [10.1126/science.277.5334.1956](https://doi.org/10.1126/science.277.5334.1956)
- 1283 Soutelino, R. G., da Silveira, I. C. A., Gangopadhyay, A., & Miranda, J. A. (2011). Is the  
1284 Brazil Current eddy-dominated to the north of 20°S?. *Geophysical Research Letters*, 38,  
1285 L03607, doi:[10.1029/2010GL046276](https://doi.org/10.1029/2010GL046276).
- 1286 Spadone, A., & Provost, C. (2009). Variations in the Malvinas Current volume transport  
1287 since October 1992. *Journal of Geophysical Research*, 114, C02002,  
1288 doi:[10.1029/2008JC004882](https://doi.org/10.1029/2008JC004882).
- 1289 Stramma, L. (1989). The Brazil Current south of 23°S. *Deep-Sea Research*, 36, 639–646.
- 1290 Stramma, L., Ikeda, Y., & Peterson, R. G. (1990). Geostrophic transport in the Brazil  
1291 Current region north of 20°S. *Deep Sea Research Part A. Oceanographic Research Papers*,  
1292 37(12), 1875 – 1886, doi:[http://dx.doi.org/10.1016/0198-0149\(90\)90083-8](http://dx.doi.org/10.1016/0198-0149(90)90083-8).
- 1293 Stramma, L. (1991) Geostrophic transport of the South Equatorial Current in the Atlantic.  
1294 *Journal of Marine Research*, 49 (2). pp. 281-294. DOI [10.1357/002224091784995864](https://doi.org/10.1357/002224091784995864).
- 1295 Todd, R. E., Chavez, F. P., Clayton, S., Cravatte, S. E., Goes, M. P., Graco, M. I., et al.  
1296 (2019). Global perspectives on observing ocean boundary current systems. *Frontiers in Marine*  
1297 *Science*, 6, doi:[10.3389/fmars.2019.00423](https://doi.org/10.3389/fmars.2019.00423).
- 1298 Tracey, K. L., Howden, S. D., & Watts, D. R. (1997). IES Calibration and Mapping  
1299 Procedures. *Journal of Atmospheric and Oceanic Technology*, 14, 1483–  
1300 1493, [https://doi.org/10.1175/1520-0426\(1997\)014<1483:ICAMP>2.0.CO;2](https://doi.org/10.1175/1520-0426(1997)014<1483:ICAMP>2.0.CO;2).
- 1301 Valla, D., Piola, A. R., Meinen, C. S., & Campos, E. (2018). Strong mixing and  
1302 recirculation in the northwestern Argentine Basin. *Journal of Geophysical Research-Oceans*,  
1303 123(7):4624-4648, doi:[10.1029/2018JC013907](https://doi.org/10.1029/2018JC013907).
- 1304 Valla, D., Piola, A. R., Meinen, C. S., & Campos, E. (2019). Abyssal transport variations  
1305 in the southwest South Atlantic: First insights from a long-term observation array at 34.5°S.  
1306 *Geophysical Research Letters*, 46(12):6699-6705, doi:[10.1029/2019GL082740](https://doi.org/10.1029/2019GL082740).
- 1307 Vivier, F., & Provost, C. (1999). Direct velocity measurements in the Malvinas  
1308 Current. *Journal of Geophysical Research*, 104(C9), 21083– 21103, doi:[10.1029/1999JC900163](https://doi.org/10.1029/1999JC900163).

- 1309 Watts, D., & Rossby, H. T. (1997). Measuring dynamic heights with inverted echo  
1310 sounders: Results from MODE. *Journal of Physical Oceanography*, 7:345–358.  
1311 ([doi:10.1175/1520-0485\(1977\)007<0345:MDHWIE>2.0.CO;2](https://doi.org/10.1175/1520-0485(1977)007<0345:MDHWIE>2.0.CO;2))
- 1312 Watts, D. R., & Kontoyiannis, H. (1990). Deep-ocean bottom pressure measurement:  
1313 Drift removal and performance. *Journal of Atmospheric and Oceanic Technology*, 7:296–306.  
1314 ([doi:10.1175/1520-0426\(1990\)007<0296:DOBPMD>2.0.CO;2](https://doi.org/10.1175/1520-0426(1990)007<0296:DOBPMD>2.0.CO;2))
- 1315 Watts, D. R., Bane, Jr., J. M., Tracey, K. L., & Shay, T. J. (1995). Gulf Stream path and  
1316 thermocline structure near 74°W and 68°W. *Journal of Geophysical Research*, 100, 18,291--18,  
1317 312.
- 1318 Weijer, W., Cheng, W., Drijfhout, S. S., Federov, A.V., Hu, A., Jackson, L. C., et al.  
1319 (2019). Stability of the Atlantic Meridional Overturning Circulation: A review and synthesis.  
1320 *Journal of Geophysical Research: Oceans*, 124. <https://doi.org/10.1029/2019JC015083>
- 1321 Welch, P. (1967). The use of fast Fourier transform for the estimation of power spectra:  
1322 A method based on time averaging over short, modified periodograms. *IEEE Transactions on*  
1323 *audio and electroacoustics*, 15(2), pp.70-73.
- 1324 Yang, H., Lohmann, G., Wei, W., Dima, M., Ionita, M., & Liu, J. (2016). Intensification  
1325 and poleward shift of subtropical western boundary currents in a warming climate. *Journal of*  
1326 *Geophysical Research-Oceans*, 121, pp. 4928-4945 . doi: 10.1002/2015JC011513
- 1327 Yang, H., Lohmann, G., Krebs- Kanzow, U., Ionita, M., Shi, X., Sidorenko, D., et al.  
1328 (2020). Poleward shift of the major ocean gyres detected in a warming climate. *Geophysical*  
1329 *Research Letters*, 47, e2019GL085868. <https://doi.org/10.1029/2019GL085868>
- 1330 Zemba, J. C. (1991). The structure and transport of the Brazil Current between 27° and  
1331 36° South, Ph.D. Thesis, Woods Hole Oceanographic Institution–Massachusetts Institute of  
1332 Technology Joint Program, WHOI Technical Report 91–37, Woods Hole Massachusetts, 160 pp.